Journal of South American Earth Sciences 112 (2021) 103534

Contents lists available at ScienceDirect

Journal of South American Earth Sciences

journal homepage: www.elsevier.com/locate/jsames

P-T-*t* path reconstruction in a syn-deformational migmatization event along the north-central portion of Sierra de Comechingones, Córdoba, Argentina

Matías G. Barzola [a,b,*], Alina M. Tibaldi [a,b], Juan E. Otamendi [a,b], Eber A. Cristofolini [a,b], Joshua J. Schwartz [c], María P. Benito [a,b], Paula Armas [a,b]

[a] Departamento de Geología, Universidad Nacional de Río Cuarto, X5804BYA, Río Cuarto, Argentina
[b] Instituto de Ciencias de la Tierra, Biodiversidad y Sustentabilidad Ambiental, CONICET-UNRC, Ruta Nacional N° 36 km 601, Río Cuarto, Argentina
[c] Department of Geological Sciences, California State University Northridge, 18111, Nordhoff Street, Northridge, CA, USA

ARTICLE INFO

Keywords:
Anatexis
Migmatites
Thermobarometry
U–Pb geochronology
Pampean orogeny

ABSTRACT

The granulite-complexes of the Sierras de Córdoba, inside context of Sierras Pampeanas, expose the deeply-uplifted internal metamorphic zone of an early Cambrian orogen. One of the largest granulite-complexes in the north-central of Sierra de Comechingones consists mainly of a set of stromatic and diatexitic migmatites all derived from metasedimentary progenitors. Migmatites vary over a spectrum of morphologies ranging from patch, net, and stromatic metatexites to schollen-schlieren and nebulite diatexites with widespread interspersed anatectic granites. The granulite-complex subordinately includes amphibolites, marbles, serpentinized ultramafic rocks, and mafic plutonic rocks. Petrographic analysis, textural and structural interpretation, thermobarometric estimates, and inherited and metamorphic zircon dating reveal the metamorphic history of migmatites in the north-central part of the Sierra de Comechingones. Metastable preservation of kyanite reflects that migmatites were buried (0.69–0.78 GPa) and heated (~650 °C) along a prograde trajectory before the onset of extensive anatexis. Then migmatites were further heated to granulite-facies peak temperatures (≥800 °C) at similar pressures (0.77 ± 0.06 GPa) through the sillimanite stability field. Widespread partial melting of the metasedimentary sequence occurred during peak metamorphism. The entire granulite-complex cooled to temperatures below 550 °C and ascended to middle crustal depths (0.3–0.5 GPa). The prograde heating trajectory and decompression during uplift overcoming cooling and tectonic exhumation are compatible with a predominantly compressive deformation. Coeval widespread partial melting with contractional non-coaxial deformation triggered self-reorganization of anatectic melts giving rise syn-deformational migmatites. In all the analyzed migmatites, U–Pb zircon geochronology yields inherited ages corresponding to those of orogenic systems that characterize the West Gondwana supercontinent. Inherited ages show a polymodal distribution pattern with contributions from Neoproterozoic (551–734 Ma; i.e., Brasiliano - Pan-African) and Mesoproterozoic detrital zircons (850–1182 Ma; i.e., Grenvillian), and minor proportions of Paleoproterozoic zircon grains (1751–1839 Ma). Ages interpreted as metamorphism and anatexis suggest the development of a single metamorphic event and restricted anatexis to a relatively short period of about 15 Ma (ca. 540-525 Ma). Metamorphic ages associated with the metamorphic peak trajectory are related to the Cambrian Pampean Orogeny.

1. Introduction

Numerous studies over the past decades showed that most of the metamorphic rocks of the Sierras de Córdoba followed a clockwise P-T path (Gordillo, 1984; Martino et al., 1994, 1995, 1997; Baldo et al., 1996; Rapela et al., 1998; Otamendi et al., 1999, 2004; Guereschi and Martino, 2002, 2008, 2014; Barzola et al., 2019a; among many others). As first inferred by pioneering studies by Gordillo (1979, 1984) the metamorphic peak attained upper-amphibolite to granulite-facies resulting in an extensive migmatitic massifs formation (Guereschi and Martino, 2014).

Gordillo (1979, 1984) was also first to recognized the geological significance of the migmatitic rocks in Sierras de Córdoba. These studies discussed that migmatites are lithological products derived from partial

* Corresponding author. Departamento de Geología, Universidad Nacional de Río Cuarto, X5804BYA, Río Cuarto, Argentina.
E-mail address: mbarzola@exa.unrc.edu.ar (M.G. Barzola).

https://doi.org/10.1016/j.jsames.2021.103534
Received 7 May 2021; Received in revised form 12 August 2021; Accepted 13 August 2021
Available online 18 August 2021

melting of metasedimentary rocks and that they constitute the deep root of an intensely eroded ancient orogen. However, there is still controversy about the nature and evolution of the anatectic process. One line of arguments suggests a continuous P-T path evolution wherein the metasedimentary sequence reached the high-grade, anatectic conditions at middle-crustal levels during the Lower Cambrian (530-520 Ma; Rapela et al., 1998); and subsequently experienced a rapid exhumation with an associated isothermal decompression (Otamendi et al., 2004; Barzola et al., 2019a,b). Alternatively, another hypothesis proposed a time gap between two partial melting events, resulting each of them, in different migmatitic rocks with distinctive mineral assemblages and structural features (Guereschi and Martino, 2008, 2014). In the latter hypothesis, cordierite-absent stromatic migmatites with prevailing S_2 foliation, termed Tala Cruz, were interpreted to be the first stage of melting. Whereas cordierite-bearing diatexites, named Cañada del Sauce, were considered decompression melting products of the prior metatexites based on the stromatic raft presence inside diatexites bodies. Supporting geochronological data of each metamorphic event is contentious due to the fact that the supposedly younger Cañada del Sauce diatexite is show to be older (577 ± 7 Ma; Siegesmund et al., 2010) than the Tala Cruz metatexite (553 ± 3 Ma; Siegesmund et al., 2010). A recent study along the Santa Rosa river pointed out that cordierite indistinctly crystallized in both metatexite and diatexite migmatites, but its stability depended on the protolith composition (Tibaldi et al., 2019). The latter study concluded that during the early Cambrian times (534-520 Ma), the diversity in the migmatic products was related to the variability on melt percent, melt distribution, and melt segregation in response to local stress field variations and subordinately to protolith variations.

This study reports petrological, structural, thermobarometric, and geochronological data of migmatites exposed over a large region from the northern Sierra de Comechingones. These migmatites make up a granulite massif stratigraphically assigned to the Calamuchita Metamorphic Complex (Otamendi et al., 2004). The main aim is to reconstruct the metamorphic P-T-*t* path by combining structural observations with thermobarometric determinations and U–Pb geochronology presented here and available from published literature. Altogether the new data enable elucidating the crustal trajectory of the migmatitic rocks in relation to the tectono-thermal evolution, which is associated with the evolution of the western margin of Gondwana during the Pampean Orogeny (Ramos, 1988; Rapela et al., 1998, 2007, 2016).

2. Regional geological background

The Sierras Pampeanas are fault-bounded N–S trending ranges of Paleozoic crystalline basement that emerged from the Cenozoic sedimentary cover. The mountain ranges were uplifted by reverse faults during the Andean orogeny in response to the flat-slab subduction of the Nazca Plate along the western margin of South America (Jordan and Allmendinger, 1986). In this context, the Sierras de Córdoba constitutes the easternmost outcrops of the Eastern Sierras Pampeanas in west-central Argentina (Fig. 1a). The Sierras de Córdoba are tilted blocks made up of an Upper Neoproterozoic-Lower Paleozoic igneous-metamorphic basement intruded by Upper Paleozoic igneous batholiths and separated by intermontane valleys filled with Mesozoic and Cenozoic sedimentary sequences (Fig. 1a; Gordillo and Lencinas, 1979; Kraemer et al., 1995; Baldo et al., 1996; Rapela et al., 1998). Schwartz et al. (2008) proposed that the basement rocks were part of a calc-alkaline, metaluminous to weakly peraluminous magmatic arc (Lira et al., 1997, 2014) in the eastern sector (Sierra Norte and southern part of Sierras Chicas; Fig. 1a); and a metasedimentary sequence equivalent to an accretionary prism (Simpson et al., 2003) in the western portion (Sierras de Pocho, Grandes, Comechingones, and central part of Sierras Chicas; Fig. 1a).

The western metasedimentary sequence is dominated by migmatites, with minor proportions of gneisses, schists, and phyllites and subordinate intercalations of amphibolites, marbles, and serpentinized ultramafic rocks (Gordillo and Lencinas, 1979; Martino et al., 1994, 2010; Baldo et al., 1996; Otamendi et al., 1999; Guereschi and Martino, 2014; among many others). Zircon and monazite geochronology document high-grade metamorphism from 553 to 514 Ma (Rapela et al., 1998; Sims et al., 1998; Gromet and Simpson, 1999; Tibaldi et al., 2008, 2019; Siegesmund et al., 2010; Ramos et al., 2015; Murra et al., 2016; D'Eramo et al., 2020; Larrovere et al., 2021, Fig. 1a). Metamorphic rocks are intruded by bimodal plutonic rocks, including both peraluminous anatectic granitoids and mafic plutonic rocks such as those outcropping in Cerro Pelado massif and Suya Taco, Sol de Mayo, and Rio Grande complexes, among others (Gordillo, 1984; Demichelis et al., 1996; Rapela et al., 1998; Schwartz et al., 2008; Tibaldi et al., 2008, 2014, 2021). U–Pb dating in zircons and monazites from anatectic granitoids brackets this magmatic activity to a brief time period between 529 and 514 Ma (Lyons et al., 1997; Rapela et al., 1998; Stuart-Smith et al., 1999; Escayola et al., 2007; Tibaldi et al., 2008; D'Eramo et al., 2020, Fig. 1a). Recently, similar U/Pb zircon ages (535-522 Ma; Tibaldi et al., 2019) were reported on anatectic granites emplaced along syn-migmatic structures in the Santa Rosa river section (Fig. 1a and b). On the other hand, there is less geochronology information available for the mafic igneous suites including gabbros, gabbronorites, ferro-gabbros, and ferro-diorites with OIB-like geochemical signature in transition to tholeiitic (Demichelis et al., 1996; Rabbia et al., 1996; Tibaldi et al., 2008, 2014, 2021, Fig. 1a and b). Ramos (1979) reported a K–Ar amphibole age of 512 ± 15 Ma (Fig. 1a); whereas U–Pb monazite dating of the contact aureole and a metasedimentary granulite-facies septa contained in mafic rocks of the northern of Sierra de Comechingones (Suya Taco and Sol de Mayo complexes respectively; Fig. 1a and b) gives ages of 520 ± 3 Ma (Tibaldi et al., 2008, Fig. 1a). Consistently, U–Pb zircon dating of OIB-like mafic rocks from central of Sierra de Comechingones (Río Grande complex; Fig. 1a and b) yield a very similar age of 520 ± 3 Ma (Tibaldi et al., 2021, Fig. 1a and b).

The most common structural feature displays by the granulite-facies metamorphic rocks is a penetrative foliation (S_2) observed as mineral banding developed during the migmatization stage (Martino and Guereschi, 2014; Tibaldi et al., 2019). The migmatitic structures show a continuous evolution during a non-coaxial progressive deformation (Barzola et al., 2019b; Tibaldi et al., 2019). The initial S_{2a} foliation, defined by leucosomes oriented parallel to the relict S_1 foliation, is progressively folded resulting in open to tight asymmetrical folds and a new S_{2b} migmatitic foliation parallel to the axial plane of the folds (Barzola et al., 2019b; Tibaldi et al., 2019). According to Martino and Guereschi (2014) these structures correspond to a composite foliation S (planar) + B (fold). High-strain rate nucleated in F_2 fold-limbs developed a strong elongation parallel to the axial plane without changes in the mineral assemblages suggesting that this deformation waned over the cooling stage (Barzola et al., 2019b; Tibaldi et al., 2019).

Post-metamorphic tectonic reworking related to crustal-scale contraction of the early Ordovician Famatinian orogeny occurred as shear zones transposing the metamorphic complexes of the Sierra de Córdoba (Martino, 2003; Otamendi et al., 2004; Steenken et al., 2010; Demartis et al., 2017). These shear zones are N–S to NNE-SSW striking with sub-vertical dips, and retain mineral assemblages re-equilibrated under greenschist-facies conditions (Martino, 2003; Simpson et al., 2003; Otamendi et al., 2004; Martino and Guereschi, 2014; Semenov and Weinberg, 2017; Radice et al., 2021).

The study area extends over 600 km^2 in the western metasedimentary sequence of the Sierras de Cordoba (Figs. 1 and 2). The granulite-facies metamorphic rocks are part of the Calamuchita Metamorphic Complex (Otamendi et al., 2004) that partially overlaps with the Sierra de Comechingones Metamorphic Complex (Martino et al., 1995). The Calamuchita Metamorphic Complex (Fig. 1b) consists of a metasedimentary sequence of stromatic migmatites and melt-depleted to melt-rich diatexites with subordinate gneiss, granulites, peraluminous leucogranites, marble/calc-silicates, amphibolites with MORB-like affinities, and metamorphosed peridotites (Otamendi et al.,

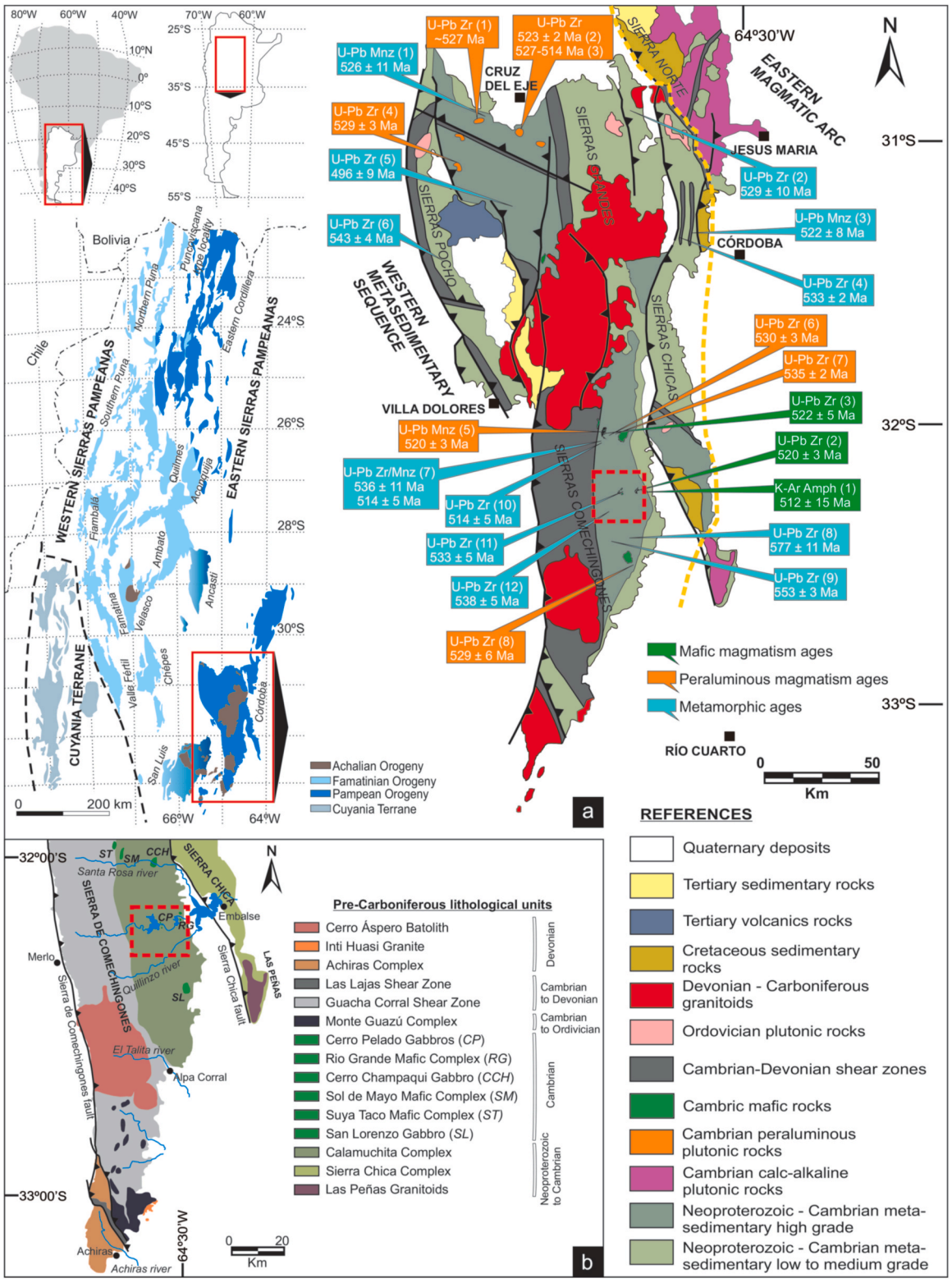

Fig. 1. a) Simplified geologic map of the Sierras de Córdoba (modified after Guereschi and Martino, 2014 and Tibaldi et al., 2021) showing the western metasedimentary sequence (Sierra Grande, Sierra de Comechingones, Sierra de Pocho, and central part of Sierras Chicas) and part of the eastern calc-alkaline magmatic arc (southern part of Sierras Chicas and Sierra Norte) outlined by the yellow dashed line. The map includes metamorphic and peraluminous and mafic magmatism ages. The geochronological data of metamorphic ages are: (1,2) Sims et al. (1998); (3,4) Rapela et al. (1998); (5,6,7,8,9) Siegesmund et al. (2010); (10) Ramos et al. (2015); (11,12) This work. The source of peraluminous magmatism ages data are: (1) Lyons et al. (1997); (2) Rapela et al. (1998); (3) Stuart-Smith et al. (1999); (4) Escayola et al. (2007); (5) Tibaldi et al. (2008); (6,7) Tibaldi et al. (2019); (8) D'Eramo et al. (2020). The age of mafic rocks are after: (1) Ramos (1979); (2,3) Tibaldi et al. (2021). The red rectangle corresponds to the study area of Fig. 2. The left box outlines the localization of Sierras de Córdoba within the context of the Eastern Sierras Pampeanas (modified after Otamendi et al., 2019) and in relation to South America and Argentina. b) Simplified geologic map of Sierra de Comechingones (modified after Otamendi et al., 2014) which includes lithostratigraphic units mentioned in the text. The red rectangle corresponds to the study area of Fig. 2. (For interpretation of the references to colour in this figure legend, the reader is referred to the Web version of this article.)

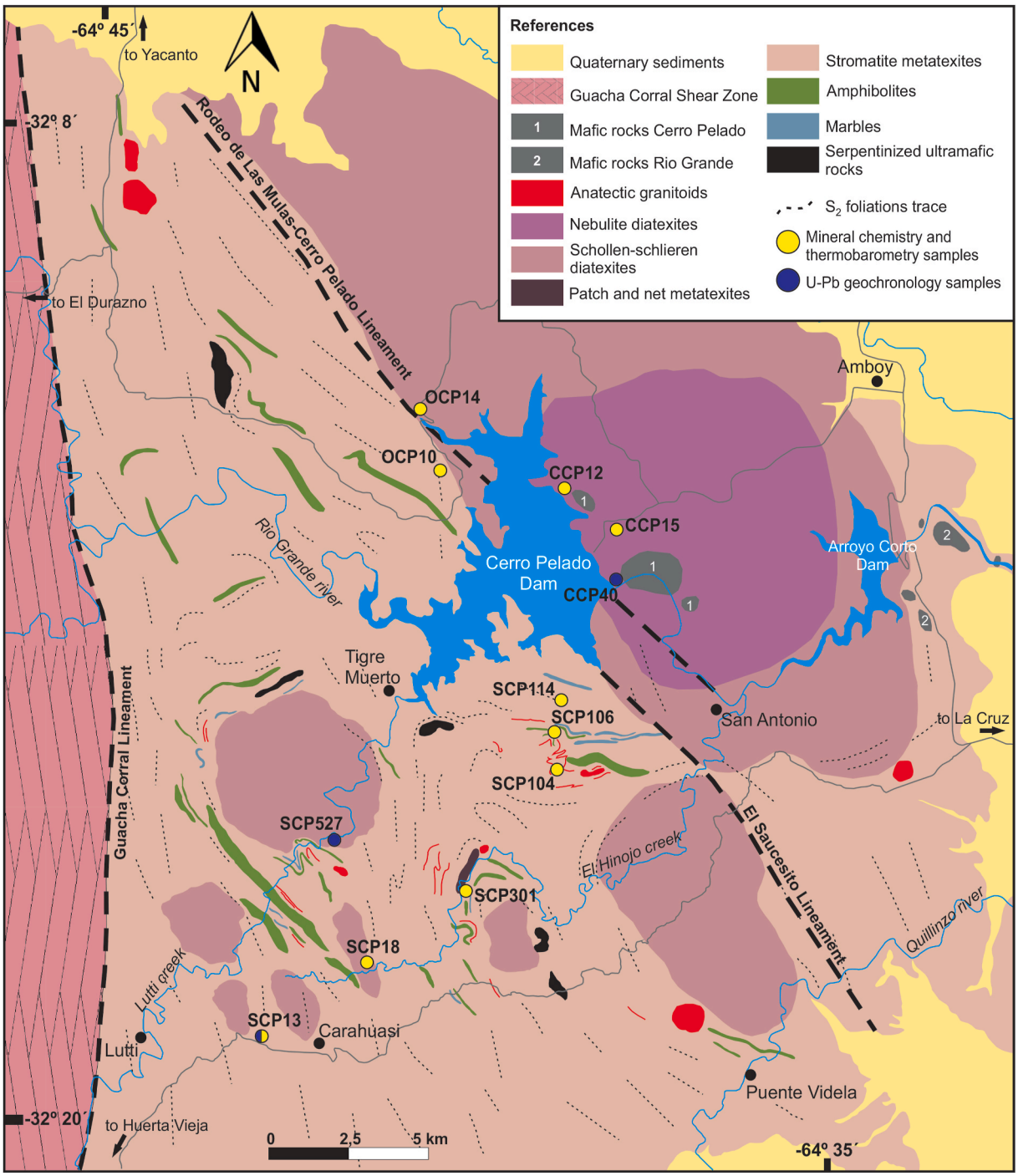

Fig. 2. Simplified geologic map of the study area taken after Barzola et al. (2019b) including localization of mineral chemistry, thermobarometry, and U–Pb geochronology samples.

2004).

3. Methodology

The classification and description of migmatites broadly follows the nomenclature proposed by Sawyer (2008). In text and figures, names abbreviation for rock-forming minerals is according to Whitney and Evans (2010).

Selected minerals from thin sections that include garnet, biotite, feldspars, and cordierite were analyzed in a JEOL JXA-8200 electron microprobe consisting of four WDS detectors in the University of Huelva (Spain). The measurement time of each element was between 10 and 30 s using a voltage potential of 15 kV, an incident ray of 5 μm to diameter, and a current of 20 nA. Natural and synthetic materials were used as standards. Obtained data were reduced through the correction of the PROZA matrix and/or with the method of Bence and Albee (1968). Mineral chemistry analyses are from four stromatic metatexites (samples SCP106b/106c/114 and OCP10), one schollen-schlieren diatexite (sample OCP14), and one nebulite diatexite (samples CCP15). In addition, we also present complementary mineral chemistry for six samples (SCP301/104b/104c/13/18 and CCP12) taken after Barzola et al. (2019a) and Otamendi et al. (2019). All chemical analyses are presented

in the supplementary material Table A1.

Thermobarometry estimates were obtained through two independent approaches. Conventional thermobarometry was performed using a set of metamorphic reactions (geothermometers and geobarometers) following the methodology of Spear (1993) and the thermodynamic standard state properties, heat capacity parameters, compressibility coefficients, and equations from Berman (1988) and Berman and Aranovich (1996). In order to account for non-ideal behavior of solid solutions were used the activity models of Berman (1988) for garnet, Holland and Powell (1992) model 1 for plagioclase, Patiño Douce et al. (1993) for biotite, and Berman and Aranovich (1996) for cordierite. P-T conditions were calculated through the following metamorphic reactions:

[R1 – Fe–Mg exchange in Bt-Grt]

$$Fe_3Al_2Si_3O_{12} + KMg_3AlSi_3O_{10}(OH)_2 = Mg_3Al_2SiO_{12} + KFe_3AlSi_3O_{10}(OH)_2$$

[R2 – Fe–Mg exchange in Grt-Crd]

$$1/3Fe_3Al_2Si_3O_{12} + 1/2Mg_2Al_4Si_5O_{18} = 1/3Mg_3Al_2Si_3O_{12} + 1/2Fe_2Al_4Si_5O_{18}$$

[R3 – GASP garnet-aluminosilicate-quartz-plagioclase]

$$Ca_3Al_2Si_3O_{12} + 2Al_2SiO_5 + SiO_2 = 3CaAl_2SiO_8$$

[R4 – GBP garnet-biotite-plagioclase]

$$3CaAl_2Si_3O_{12} = Al_2(Mg,Fe)_{-3} + CA_3Al_2Si_3O_{12} + (Mg,Fe)_3Al_2Si_3O_{12}$$

The second procedure performs multi-equilibria calculation using the software THERMOCALC and the internally consistent thermodynamic database of Holland and Powell (2011). In THERMOCALC, the mineral activities were determined with Tim Holland's AX62 program (last update in February 2019).

U–Pb zircon geochronology was performed in three representative samples (SCP13, SCP527, and CCP40). Zircons were separated from whole-rock, which included both melanosome and leucosome, following standard methods that include the crushing, milling, and magnetic-heavy liquids separation.

Samples SCP13 and SCP527 were analyzed in the ChronusCamp Research laboratories (http://www.chronuscamp.com/index.html). Cathodoluminescence images (CL) were made from handpicked zircons and mounted in epoxy using an FEI Quanta 250 scanning electron microscope. U–Pb ratios were measured using a laser ablation system coupled to a plasma emission and mass spectrometry system (LA-ICP-MS). To optimize the analysis, the laser operated at 7 Hz generating an ablation spot of ~30 μm of diameter. GJ-1 zircons (Jackson et al., 2004) were used as primary standards measured every 10 unknown analyses in order to correct for Pb/U fractionation and Pb isotopes during routine. Plešovice (Slama et al., 2008) was used as a secondary standard in order to assess the reproducibility of the data.

Sample CCP40 was analyzed at the California State University (USA). Zircons were handpicked and mounted in epoxy were imaged with a Gatan MiniCL detector attached to an FEI Quanta 600 electron microscope. Uranium-lead ratios were collected using a ThermoScientific Element2 SF-ICP-MS coupled to a Teledyne Cetec Analyte G2 Excimer Laser which was operated at a wavelength of 193 nm. Furthermore, beam diameter was 25 μm with an ablation depth of 20–30 μm, being operated with a power of 10 Hz. 91,500 zircons (Wiedenbeck et al., 1995, 2004) were used as the primary standard and was analyzed every 10–15 unknown analyses. Temora 2 zircons (Black et al., 2004) were employed as a secondary standard.

Reduction of the analytical data was performed using the Iolite software (Paton et al., 2011) in both laboratories. The final data processing and plotting was carried out with Isoplot 3.0 (Ludwig, 2003). A discordance filter was applied whereby we excluded analyses with more 30% of discordance (< 70% in concordance comparing $^{206}Pb/^{238}U$ and $^{206}Pb/^{207}Pb$ ages), more than 5% of inverse discordance (< 105% in concordance), and $^{206}Pb/^{238}U$ ages less than 500 Ma with large uncertainties (Gehrels et al., 2008). Simultaneously, since usually an increase in the uncertainty of $^{206}Pb/^{238}U$ ages occurs at the same time that decreases uncertainty in $^{206}Pb/^{207}Pb$ ages as a function of age (Williams, 1998); $^{206}Pb/^{238}U$ ages were considered for <900 Ma and $^{206}Pb/^{207}Pb$ ages for >900 Ma. Analytical data are reported in the supplementary material Table A2.

4. Results

4.1. Morphology, field description and petrography of the migmatic rocks

The study area consists of early Paleozoic crystalline metamorphic rocks of prevailing migmatites and anatectic granites with subordinate outcrops of mafic plutonic rocks (Barzola et al., 2019a, Fig. 2). The migmatic rocks encompass a complete range from metatexites to diatexites formed during a single high-grade metamorphic event. According to their internal structures, migmatites vary among patch, net, and stromatic metatexites to schollen-schlieren and nebulite diatexites (Figs. 2 and 3).

Patch and net metatexites are locally found in the south-central sector of the study area (Fig. 2). This rock type outcrops as few meters thick tabular bodies showing well-defined contacts with stromatitic migmatites. The paleosome consists of a medium-grained mesocratic gneissic rock with granolepidoblastic texture showing millimeter-thick layering (Fig. 3a). It is composed of quartz, plagioclase, dark brown to greenish biotite, and pink garnet with numerous quartz, biotite, and opaque minerals inclusions in the core of the crystals. The neosome is leucocratic, medium-to coarse-grained size, and with equigranular texture (Fig. 3a). It consists of patches of dispersed melt that coalesce forming a rhombohedra-style network of interconnected leucosomes around the relict paleosomes (Fig. 3a). The neosome contains quartz, plagioclase, K-feldspar, garnet (located in the center of the melt patches and leucosomes), and very scarce dark brown to reddish biotite. Accessory minerals common to both paleosome and neosome are zircon, monazite, apatite, and Fe–Ti oxides.

Stromatic metatexites are the most abundant rocks in the study area (Fig. 2). They mainly outcrop as tabular bodies, although locally, when the volume fraction of leucosome increases exhibit sub-rounded morphologies. This rock type displays clear separation of leucosome-melanosome pair in plane-parallel to folded layers (Fig. 3b). However, it is sometimes observed a relict mesocratic gneissic paleosome. Paleosome appears as tabular bodies, up to 2 m long and 50 cm in thick (Fig. 4a), with millimeter-thick layers of alternating medium-grained granoblastic and fine-grained lepidoblastic textural domains. The typical paleosome mineral assemblage is quartz, plagioclase, pale to dark brown biotite, and scarce garnet with zircon, monazite, apatite, and Fe–Ti oxides as accessory minerals.

According to their mineralogical composition, stromatic metatexites are subdivided into Kfs + Grt and Kfs + Grt + Sil ± Crd varieties (Fig. 4a). All stromatic metatexites have up to 5 cm thick leucosomes with medium to coarse granular texture interspersed with 2–7 cm thick medium-to coarse-grained granolepidoblastic melanosomes. Additionally, Kfs + Grt + Sil ± Crd stromatite develops porphyroblastic texture, and a thin (1–2 mm) biotite-rich mafic selvedge usually appears between the leucosome-melanosome pairs. Leucosomes in stromatites are dominated by quartz and plagioclase with variable K-feldspar proportions, sporadic inclusions-free idiomorphic fine-grained garnets, and a few reddish brown biotites. In contrast, melanosomes are made up of reddish brown biotite, quartz, plagioclase, and idiomorphic to xenomorphic garnet; whereas minor proportions of sillimanite, and less frequently cordierite also occur in Kfs + Grt + Sil ± Crd stromatites (Fig. 3c). Plagioclases of leucosomes show myrmekite textures and K-feldspars are micro-to mesoperthitic. Biotites usually display intergrowths with quartz, and locally present internal exsolution of acicular rutiles.

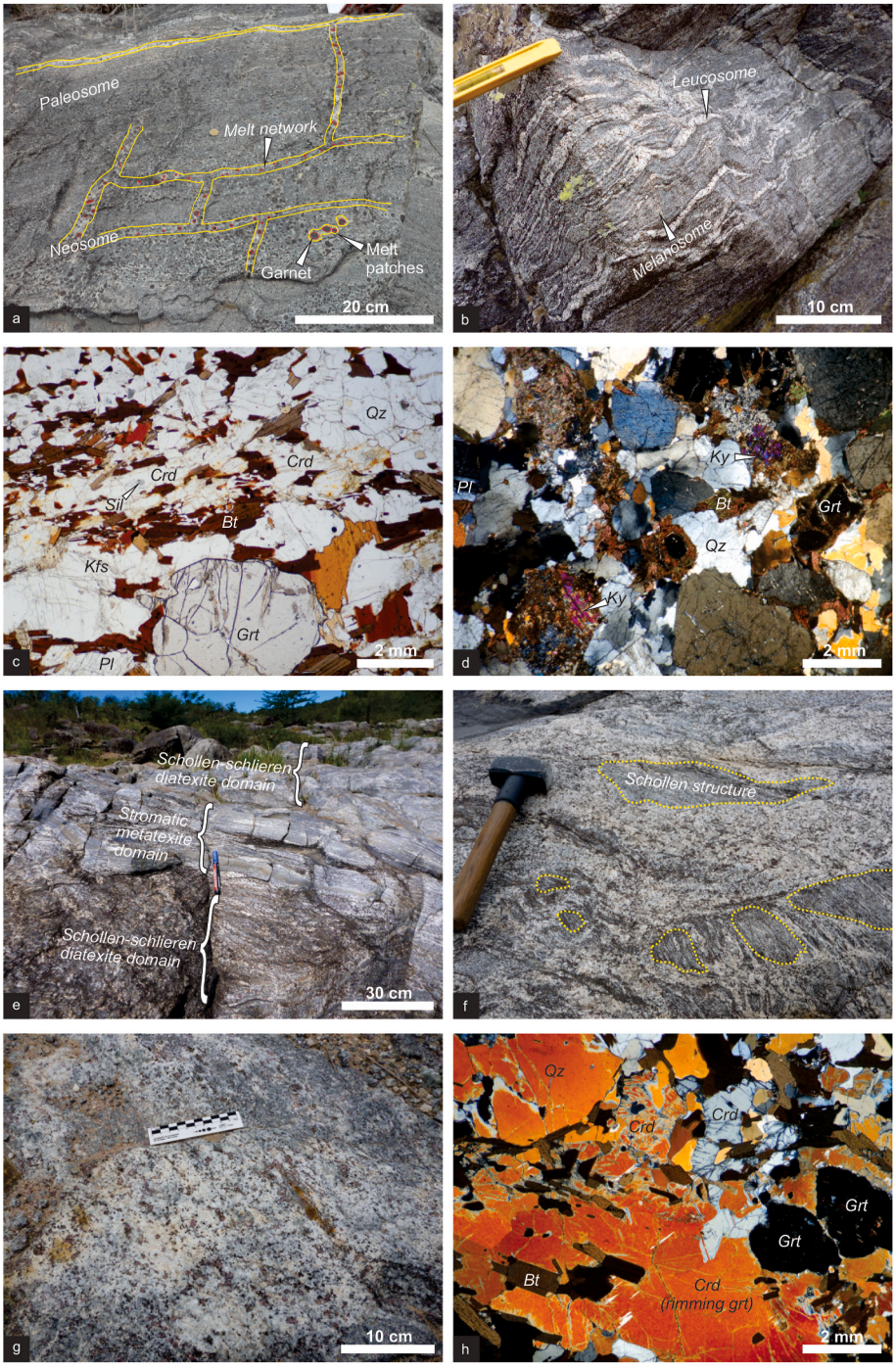

Fig. 3. a) Patch and net metatexite showing patches of leucosome and a rhombohedra shaped network of interconnected leucosomes around the relict paleosome. b) Stromatic metatexite with the leucosome-melanosome pair folded in open folds. c) Photomicrograph of Kfs + Grt + Sil ± Crd stromatites displaying cordierites as coarse-grained xenoblasts elongated parallel to the biotite-garnet-rich layers. d) Photomicrograph of Kfs + Grt + Sil ± Crd stromatite showing a relict kyanite grain. e) Transitional contact between stromatic metatexite and schollen-schlieren diatexite. f) Stromatic rafts included inside schollen-schlieren diatexite that is oriented parallel to an internal mineral orientation of the diatexite rock displayed by phyllosilicates and feldspars. g) Leucocratic nebulite diatexite where pre-anatectic structures are completely replaced by a magmatic-type diatexitic foliation. h) Photomicrograph of mesocratic nebulite diatexite showing cordierites as both peritectic xenoblasts altered to pinnite and pristine cordierite surrounding garnet.

Garnets show inclusions of biotite and quartz in their cores and occasionally, in the Kfs-Grt-Sil-Crd stromatites type, fine-grained sillimanite needles in their rims. Also, locally some garnets are partially surrounded by biotite which in turn may partially transform to chlorite. Sillimanite appears either as well-defined prisms associated with garnet and biotite or as fine needles in plagioclase or cordierite. Locally, relict kyanite is part of the mineral assemblage in stromatic migmatites from the east edge of the Cerro Pelado dam (Fig. 3d). Cordierite occurs as coarse-grained xenoblasts elongated parallel to the biotite-garnet-rich layers (Fig. 3c). Sporadically cordierite is partially rimming to garnet. The most common accessory minerals in both types of stromatites are zircon, monazite, apatite, and Fe–Ti oxides.

Schollen-schlieren diatexites are sub-rounded bodies which display transitional contact, at outcrop scale, with metatexite rocks (Fig. 3e). They exhibit granular to porphyric texture and medium-to coarse-grained size. These diatexites are characterized by the presence of abundant irregular remnants of stromatic metatexites comprising centimeter-to meter-sized schollen (Fig. 3f), which often are disintegrated into biotite-schlieren. These structures are usually arranged parallel to an internal mineral orientation displayed by phyllosilicates and feldspars, evidencing bulk magmatic flow (Fig. 3f). The mineral assemblage includes quartz, plagioclase with myrmekite texture, microperthitic to mesoperthitic K-feldspar, reddish brown biotite, subidiomorphic to idiomorphic garnet, scarce sillimanite, and sporadic xenoblasts of cordierite. Garnet cores contain numerous inclusions of biotite and quartz, whereas the rims are usually inclusions-free or

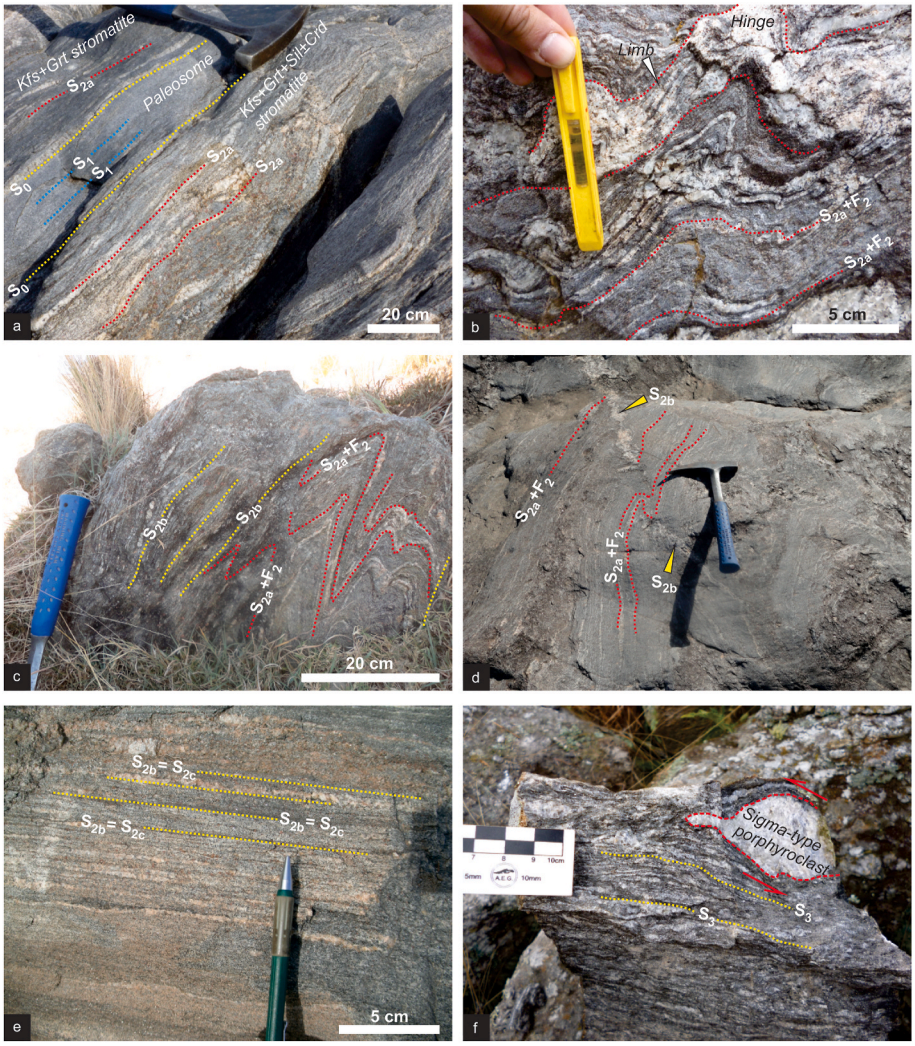

Fig. 4. a) Stromatic metatexite with S_{2a} stromatic layering preserving the compositional banding inherited from a relict S_0 primary bedding. Note in the paleosome the preservation of an internally S_1 metamorphic foliation. b) Example of S_{2a} stromatic layering disturbed by F_2 folds showing thickened hinges and thinned forelimbs. c) Fold formed by progressive tightening of S_{2a} + F_2 folded stromatic foliation (on the right side) that ends up with the generation of the S_{2b} axial plane foliation (on the left side). d) S_{2a} + F_2 folded stromatic foliation truncated by the S_{2b} axial plane foliation giving rise to sub-parallel to parallel melt migration with respect to the fold axial plane. e) S_{2c} high-temperature shear foliation, generated under amphibolite-to granulite-facies, oriented parallel to a S_{2b} axial plane foliation that generates penetrative millimeter-layering. f) Metatexite with S_3 mylonitic fabric showing quartz-feldspathic aggregates as σ-type porphyroclasts.

sometimes develop tiny sillimanite needles. Secondary biotite partially surrounds and replaces some garnets. Biotite often shows local exsolutions of acicular and/or nodular rutile. Cordierite is peritectic and appears in contact with garnet, biotite, and felsic minerals. Zircon, monazite, apatite, and Fe–Ti oxides are conspicuous accessory minerals.

Nebulite diatexites occur as globate bodies resembling a granitic landscape. These diatexites are homogeneous and present a magmatic foliation given by the orientation of feldspars and cordierites. Small rafts of stromatic metatexites and biotite schlieren, plus elongated and irregular centimetric to metric mafic intrusives are generally arranged parallel to this magmatic foliation (Tibaldi et al., 2021). Less frequently, mafic dykes are also observed (Tibaldi et al., 2021). Diatexites vary from equi-to inequigranular rocks, and are even locally porphyric, with coarse to medium grain size. Based on the mineral assemblages, two subtypes of nebulite diatexites are distinguished. A subordinate proportion is a leucocratic nebulite (Fig. 3g) made up of quartz, plagioclase with abundant myrmekite textures, mesoperthitic K-feldspar, reddish brown biotite, idiomorphic to subidiomorphic garnet, and sporadic sillimanite. Occasionally, leucocratic nebulites develop K-feldspars idiomorphic megacrystals and partial biotite replacement along the garnet fractures and edges. The dominant diatexites are mesocratic nebulites displaying schollen/schlieren structures. Mesocratic nebulites consists of quartz, plagioclase, micro-to mesoperthitic K-feldspar, laths of reddish-brown biotite, idiomorphic to subidiomorphic garnet, abundant cordierite, and scarce sillimanite. Plagioclase commonly develops myrmekite texture, and biotite locally shows nodular to acicular rutile exsolutions. Garnet usually presents quartz, biotite and opaque minerals as core-inclusion, as well as acicular sillimanite at their rims. Cordierite appears with distinct textural relationships (Fig. 3h). One type of cordierite occurs as peritectic xenoblasts with felsic minerals commonly pinnitized (Fig. 3h). Another cordierite type surrounds garnets and is mostly pristine (Fig. 3h). Accessory mineralogy is common to both subtypes of diatexites and consists in zircon, monazite, apatite, and Fe–Ti oxides.

Anatectic granitoids derived from partial melting of the metasedimentary country rocks and have granitic to tonalitic compositions (Otamendi et al., 2019). They are spatially associated with metatexite migmatites and occur as centimeter-to several meter-wide dikes and sills (Fig. 2). Less frequently, anatectic granites occur as globular bodies of a few tens meters in diameter. Typically, they vary from medium-grained to pegmatitic-type rocks, with equigranular to inequigranular hypidiomorphic texture. Sometimes, a magmatic foliation given by the orientation of phyllosilicates and feldspars is recognized. Anatectic granites are quartz and plagioclase-rich with variable amounts of K-feldspar, biotite, garnet, muscovite, sillimanite, and cordierite. Scarce zircon, monazite, apatite, and Fe–Ti oxides are accessory minerals.

4.2. Sequence of structures

Here we summarized the most relevant structural features while a detailed description was presented elsewhere (Barzola et al., 2019b). The oldest discernible fabric in the area is a relict primary bedding (S_0)

given by an interspersed of compositional layers, which are defined by changes in modes and mineral assemblages resulting in Kfs + Grt and Kfs + Grt + Sil ± Crd stromatites (Fig. 4a). It has been shown that the primary bedding corresponds to compositional variation in the sedimentary precursors which varies from quartz-to aluminous-greywackes (Otamendi and Patiño Douce, 2001; Barzola et al., 2019a; Otamendi et al., 2019). Furthermore, an early metamorphic foliation (S_1), observed as millimeter banding (Fig. 4a) and produced by metamorphic segregation in sub-solid state, is preserve in paleosomes and refractory layers of migmatitic rocks. Both S_0 and S_1 pre-migmatitic fabrics are locally recognized, but most of these early structures have been almost entirely obliterated by partial-melting processes associated with granulite-facies metamorphism (Barzola et al., 2019b).

The S_2 syn-migmatic fabrics are dominant throughout the study area (Barzola et al., 2019b). The earliest migmatitic fabric is characterized by a continuous stromatic layering (S_{2a}) defined by segregation of leucosome-melanosome pairs arranged parallel to the prior S_1 gneissosity (Fig. 4a). This stromatic banding is disturbed by a heterogeneous fold system (F_2) which has wavelengths ranging from a few centimeters to several hundred meters. F_2 folds evolved from open, parallel and symmetrical to upright, tight/isoclinal, and asymmetric with thickened hinges and thinned forelimbs (Fig. 4b and c). Fold-axes plunge 38° to northeast whereas the limbs trends between N330° and N40° with moderate to highly dipping to the east (45°–75°), and locally high angle (75°–80°) to the west. Progressive tightening of the folded S_{2a} stromatic fabric ends up in the generation of a new migmatitic foliation (S_{2b}) nucleated parallel to the axial plane of the F_2 folds (Fig. 4c and d). As a result, S_{2b} is recognized from folded layers truncations (Fig. 4c), which originate cleavage surfaces, and melt migration parallel or sub-parallel to the folds axial plane (Fig. 4d) with N–S trending (N355°-N5°) and moderate east-dipping (40°).

Locally, high-strain deformation led to development of discrete ductile shear zones. Along these surfaces both texture and microstructure were reworked generating a high-temperature (amphibolite/granulite facies) shear foliation (S_{2c}), but still preserving the migmatitic mineral assemblage. The S_{2c} high-temperature shear foliation shows the development of garnet porphyroclasts, transformation of sillimanite in fibrolite, and generation of sigmoidal S–C structures that progressively rotate until making a strongly penetrative millimeter-layering wherein S_{2b} become parallel to S_{2c} (Fig. 4e). S_{2c} high-temperature shear foliation trends between N340°-N30° with a moderate average dipping to the east (45–50°). L_2 mineral lineation, displayed on S_{2c} surface, has an average plunging of 45° to the northeast. Taken together, the set of migmatitic structures suggests a strongly non-coaxial compressive deformation with west-verging and slightly dextral sense component (Barzola et al., 2019b).

Migmatitic structures have been locally reworked by a variably developed post-migmatitic mylonitic deformation. Mylonitic deformation is nucleated in centimetric to metric shear bands that are characterized by the development of σ-type porphyroclasts formed by garnets and quartz-feldspathic aggregates, the generation of brittle-ductile S–C structures, strong reduction of size grain rock, and partial retrograde of migmatitic mineral assemblage to muscovite + chlorite association (Fig. 4f). This textural, microstructural, and mineral reworked result in an S_3 mylonitic and post-migmatitic fabric developed under amphibolite-to greenschist-facies conditions. S_3 mylonitic fabric has N–S trending (N350°-N20°) with an average dipping of 60° to the east. L_3 mineral lineation plunges 40°–50° to E-SE (90°–120°). Structural markers of shear sense yield a compressive stress with an inverse and slightly sinistral movement with west-verging (Barzola et al., 2019b).

4.3. Mineral chemistry and thermobarometry of anatectic rocks

4.3.1. Patch and net metatexites

Chemically, garnets from patch and net metatexite differ from garnets of other migmatitic rock types, because typically develop zoned profiles (Fig. 5a). The almandine [X_{Alm} = Fe/(Fe + Mg + Ca + Mn)] and pyrope [X_{Pyp} = Mg/(Fe + Mg + Ca + Mn)] end-members increase rimwards (X_{Alm} = 0.73 to 0.76 and X_{Pyp} = 0.11 to 0.14), whereas grossular [X_{Grs} = Ca/(Fe + Mg + Ca + Mn)] and spessartine [X_{Sps} = Mn/(Fe + Mg + Ca + Mn)] decrease in the same directions (X_{Grs} = 0.10 to 0.09 and X_{Sps} = 0.05 to 0.02) suggesting growth during metamorphic prograde (Yardley, 1977, Fig. 5a). Micas are mostly biotite (Fig. 5b; Deer et al., 1993), but they are divided according to their chemical composition and textural position into two groups. Biotite included in garnet cores has low Ti contents (0.12 a. f.u.), a medium X_{Mg} [0.48 with X_{Mg} = Mg/(Mg + Fe)], and Al^{IV} and Al^{VI} contents of 1.33 a. f.u. and 0.16 a. f.u., respectively (Fig. 5c–f). Contrarily, biotite of the matrix mineral assemblage has relatively high Ti (0.22–0.24 a. f.u.) and Al^{IV} (1.36–1.38 a. f.u.) contents, but low amounts of Al^{VI} (0.10–0.14 a. f.u.) and magnesium molar fraction (X_{Mg} ~ 0.4; Fig. 5c–f). Plagioclase is oligoclase with compositions varying over a narrow range ($Ab_{70-72}An_{26-29}Or_{1-2}$; Fig. 5g) excluding a single data with andesine composition ($Ab_{67}An_{32}Or_1$; Fig. 5g).

Thermobarometric calculations were performed taking into account the chemical variation across the garnet profile (Fig. 5h and Table 1). First, and considering the paleosome mineral assemblage (Qz + Pl + Bt ± Grt), P-T conditions were estimated by linking the garnet core compositions, with the compositions of the biotite included in them, and the plagioclases with lower anorthite content. Bt-Grt thermometer (R1 reaction) yielded equilibrium temperatures of 619 ± 30 °C; whereas the GBP barometer (R4 reaction) gave estimated pressures of 0.69 ± 0.02 GPa (Fig. 5h and Table 1). Instead, for garnet rim compositions, R1 reaction adjust by R4 reactions yielded temperatures of 790 ± 25 °C (Fig. 5h and Table 1) for pressures of 0.84 ± 0.05 GPa (GBP barometer; Fig. 5h and Table 1), considering the mineral assemblage Qz + Pl + Kfs + Grt ± Bt developed in the neosome.

Given the lack of alumina polymorph in the mineral assemblage, the GASP barometer (R3 reaction) cannot be applied and multi-equilibria calculation introduces a large uncertainty. The presence of relict kyanite together with sillimanite in nearby rocks is interpreted to reflect that the metamorphic sequence could have evolved within the kyanite stability field before anatexis. Whereas peritectic sillimanite provides evidence for anatexis occurred within the sillimanite stability field. In theory, P-T estimates assuming alumina saturation of the mineral assemblage yield maximum P-T results (Patiño Douce et al., 1993). As it is well accepted, applying GASP barometer and multi-equilibria calculation in alumina polymorph-absent rocks provides an independent test for other barometers. Consistently, GASP barometer yields a maximum pressure of 0.83 ± 0.03 GPa for garnet cores analyses and 0.98 ± 0.07 GPa for the rims (Fig. 5h and Table 1); whereas P-T conditions of 645 ± 34 °C - 0.78 ± 0.04 GPa and 735 ± 43 °C - 0.78 ± 0.05 GPa (Fig. 5h and Table 1) were achieved respectively using multi-equilibria calculations (THERMOCALC).

4.3.2. Stromatic metatexites

The mineral chemistry of the stromatic metatexites is heterogeneous at regional scale, and its variability correlates to the degree of preservation of structural features that predate morphological reorganization during anatexis. A first group of stromatic metatexites, which are similar to bedded migmatites in Otamendi et al. (2019), are characterized by preserving the compositional banding inherited from relict S_0 primary bedding interpreted to be the alternation of quartz-metagreywacke and aluminous-metagreywacke beds of the sedimentary package (Otamendi and Patiño Douce, 2001; Barzola et al., 2019a; Otamendi et al., 2019). In both layers, the garnet compositions are dominated for almandine end-member (X_{Alm}) with less proportions of pyrope (X_{Pyp}) and minor grossular (X_{Grs}) and spessartine (X_{Sps}) contents (Fig. 6a and b). In particular, garnet of quartz-metagreywacke layers has an almost flat compositional zoning pattern ($Alm_{66-69}Pyp_{26-28}Grs_{2-3}Sps_{2-3}$; Fig. 6a), typical of diffusion processes at high-grade conditions (Yardley, 1977). Whereas, garnet of aluminous-metagreywacke layers shows a

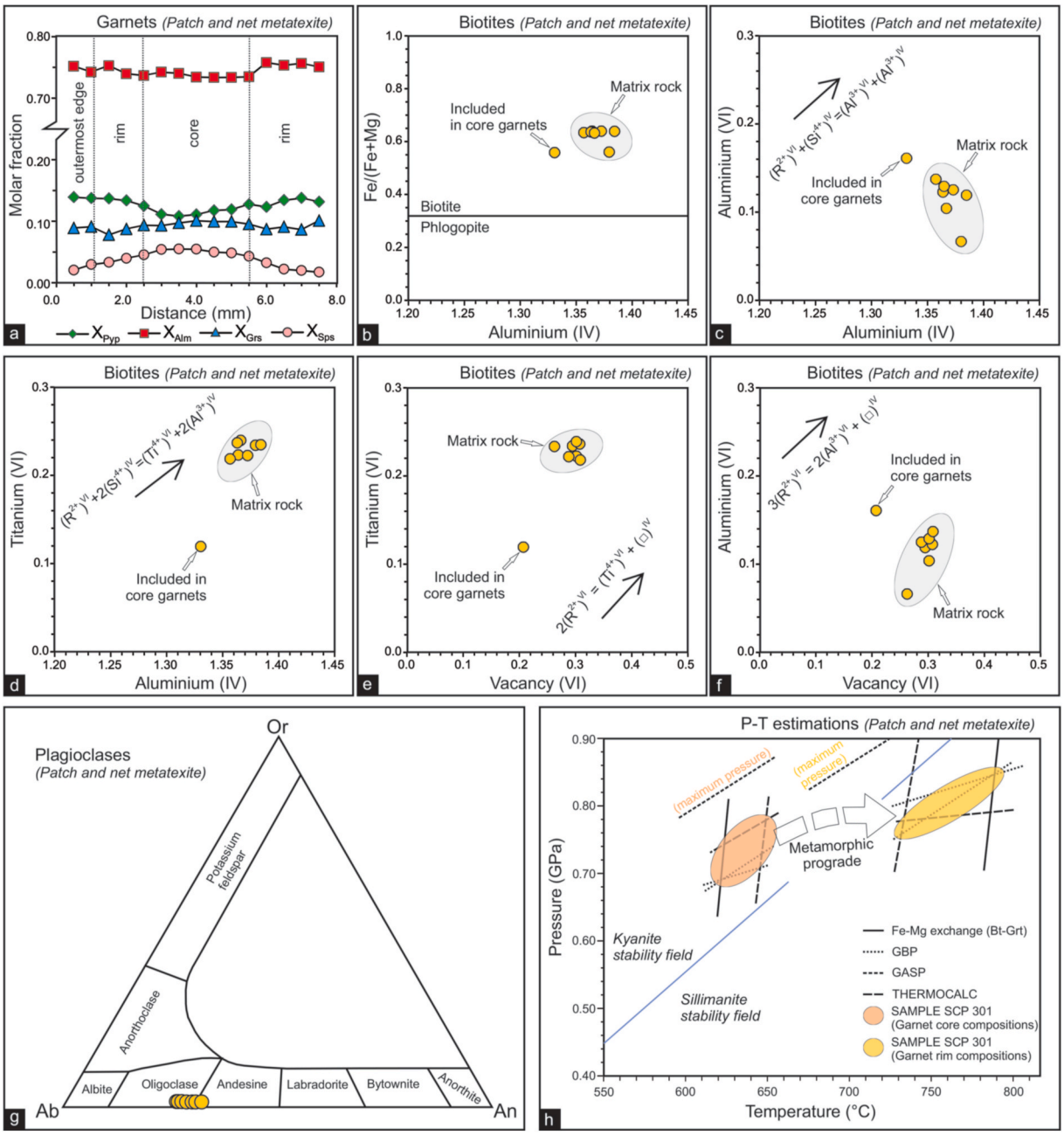

Fig. 5. Mineral chemistry of patch and net metatexites. a) Compositional garnet profile. b) Classification of micas taken after Deer et al. (1993). c) Aluminium (IV) vs. Aluminium (VI), d) Aluminium (IV) vs. Titanium (VI), e) Vacancy (VI) vs. Titanium (VI), and f) Vacancy (VI) vs. Aluminium (VI) diagrams. The arrow indicates the direction of ion-exchange vector. g) Anorthite-Albite-Orthoclase ternary diagram. h) P-T diagram showing the equilibrium conditions estimated from integrating the P-T estimates. The P-T stability of alumina polymorphs is after Pattison (1992).

compositional profile in almandine and pyrope end-members with almost constant compositions (X_{Alm} = 0.68–0.70 and X_{Pyp} = 0.25–0.26) in a wide core zone, and increase in almandine (X_{Alm} = 0.74) and decrease in pyrope (X_{Pyp} = 0.21) components towards the rims (Fig. 6b), suggesting a chemical homogeneity at peak conditions followed by retrograde in Fe/Mg exchange reaction (Kohn and Spear, 2000). Biotite in both layers is Ti-rich (0.22–0.31 a. f.u.) with X_{Mg} between 0.58 and 0.71, and Al^{IV} and Al^{VI} content varies around 1.29–1.36 a. f.u. and 0.21–0.33 a. f.u., respectively (Fig. 6c–f). Plagioclase is oligoclase with compositions $Ab_{76\text{-}73}An_{22\text{-}23}Or_{2\text{-}4}$ for quartz-metagreywacke layers and $Ab_{77\text{-}78}An_{22\text{-}21}Or_{1}$ for aluminous-metagreywacke layers (Fig. 6g). Alkali feldspar has $Ab_{12\text{-}17}An_{1}Or_{83\text{-}87}$ compositions (Fig. 6g).

P-T estimates were performed considering the mineral assemblages Qz + Pl + Bt + Grt ± Kfs for the quartz-metagreywacke layers (samples SCP104c and SCP106c), and Qz + Pl + Kfs + Bt + Grt + Sil for the aluminous-metagreywacke layer (sample SCP104b). Thus, for the wide core zone of the garnet in the aluminous-metagreywacke layer (SCP104b), intersections of R1, R3 and R4 reactions give equilibrium conditions of 765 ± 20 °C for pressures between 0.76 ± 0.03 GPa (GBP barometer) and 0.69 ± 0.04 GPa (GASP barometer; Fig. 6h and Table 1). These results are consistent with the estimates applying THERMOCALC, which yield a little higher temperature value (810 ± 72 °C) within the same pressures range (0.73 ± 0.05 GPa; Fig. 6h and Table 1). On the other hand, in the quartz-metagreywacke layers (samples SCP104c and SCP106c), the convergence of R1 thermometer and R4 barometer yielded average temperatures and pressures of 745 ± 35 °C - 0.65 ± 0.03

Table 1
Summary of thermobarometric estimates.

Sample	Type rock	Mineral assemblage	Mineral spot	Conventional thermobarometry				Multi-equilibria thermobarometry	
				Fe–Mg (Bt-Grt)	Fe–Mg (Grt-Crd)	GASP	GBP	THERMOCALC	
				T (°C)	T (°C)	P (GPa)	P (GPa)	T (°C)	P (GPa)
SCP 301	PNM	Qz + Pl + Bt ± Grt	Core-grt	619 ± 30		0.83 ± 0.03	0.69 ± 0.02	645 ± 34	0.78 ± 0.04
		Qz + Pl + Kfs + Grt ± Bt	Rim-grt	790 ± 25		0.98 ± 0.07	0.84 ± 0.05	735 ± 43	0.78 ± 0.05
SCP 104b	SM (As)	Qz + Pl + Kfs + Bt + Grt + Sil	Core-grt	765 ± 20		0.69 ± 0.04	0.76 ± 0.03	810 ± 72	0.73 ± 0.05
SCP 104c	SM (Qz)	Qz + Pl + Bt + Grt ± Kfs	Core-grt	715 ± 30			0.63 ± 0.03	815 ± 67	0.68 ± 0.04
SCP 106c	SM (Qz)			775 ± 25			0.67 ± 0.03	800 ± 56	0.67 ± 0.03
OCP 10	SM	Qz + Pl + Kfs + Bt + Grt ± Sil	Core-grt	760 ± 25		0.76 ± 0.03	0.76 ± 0.02	825 ± 45	0.77 ± 0.07
			Rim-grt	500 ± 30		0.31 ± 0.04	0.34 ± 0.03	555 ± 70	0.47 ± 0.15
SCP 13	SM	Qz + Pl + Kfs + Bt + Grt ± Sil	Core-grt	795 ± 25		0.78 ± 0.02	0.8 ± 0.02	820 ± 62	0.77 ± 0.01
			Rim-grt	555 ± 35		0.42 ± 0.04	0.43 ± 0.02	520 ± 65	
SCP 114	SM	Qz + Pl + Kfs + Bt + Grt ± Sil	Core-grt	800 ± 35		0.74 ± 0.06	0.82 ± 0.05	828 ± 54	0.8 ± 0.05
SCP 106b	SM	Qz + Pl + Kfs + Bt + Grt + Crd ± Sil	Core-grt	810 ± 20	775 ± 40	0.68 ± 0.07	0.77 ± 0.06	800 ± 55	0.81 ± 0.07
OCP 14	SSD	Qz + Pl + Kfs + Bt + Grt ± Sil	Core-grt	820 ± 30		0.67 ± 0.06	0.74 ± 0.04	815 ± 54	0.79 ± 0.15
SCP 18	SSD			855 ± 55		0.68 ± 0.05	0.74 ± 0.05	835 ± 65	0.78 ± 0.08
CCP 12	ND	Qz + Pl + Kfs + Bt + Grt + Crd + Sil	Core-grt	755 ± 55	780 ± 35	0.56 ± 0.07	0.63 ± 0.05	855 ± 55	0.66 ± 0.1
CCP 15	ND			805 ± 30	785 ± 30	0.6 ± 0.06	0.71 ± 0.05	850 ± 59	0.67 ± 0.09

Note: PNM: Patch and net metatexite; SM (As): Stromatic metatexite (Aluminous-metagreywacke layer); SM (Qz): Stromatic metatexite (Quartz-metagreywacke layer); SM: Stromatic metatexite; SSD: Schollen-schlieren diatexite; ND: Nebulite diatexite.

GPa (Fig. 6h and Table 1). The lack of alumina polymorph in stromatic migmatites may bias the results of multi-equilibria calculations. However, the presence of sillimanite in the interbedded aluminous-metagreywacke layer (sample SCP104b) is taken to reflect that the entire migmatic sequence evolved within the sillimanite stability field. Following these arguments, THERMOCALC estimations were done assuming that sillimanite was stable. In both samples, equilibrium conditions give slightly higher temperature values at the same pressure range with respect to conventional thermobarometry (Fig. 6h and Table 1). These results are within the error range of P-T determinations in the adjacent aluminous-metagreywacke layer (sample SCP104b).

In a second group of stromatites, pre-migmatic fabrics have been obliterated and replaced by syn-migmatic fabrics. Garnet composition varies from $Alm_{66-69}Py_{25-28}Grs_{4-5}Sps_2$ in the core to $Alm_{71-76}Py_{16-18}Grs_3Sps_3$ rimwards (Fig. 7a), showing a zoned profile typically assigned to ion-exchange during cooling (Kohn and Spear, 2000). Micas are mostly biotite (X_{Mg} = 0.50–0.65) with minor proportion of phlogopite (X_{Mg} ~ 0.73). In general, both are rich in Ti (0.16–0.29 a. f.u.; Fig. 7d and e) and the Al^{IV} content range between 1.25 and 1.35 a. f.u., whereas Al^{VI} varies over a wide range (0.22–0.40 a. f.u.; Fig. 7c and f). Plagioclase is oligoclase to andesine with $Ab_{65-73}An_{26-34}Or_{1-2}$ compositions (Fig. 7g). Alkali feldspar is orthoclase ($Ab_{11-15}An_{1-2}Or_{83-89}$; Fig. 7g) and usually has perthitic albite-rich intergrowths ($Ab_{97}An_3Or_1$; Fig. 7g). Cordierite has a uniform X_{Mg} ranging between 0.73 and 0.75.

P-T estimates were performed using both core and rim garnet compositions, and considering the mineral assemblages Qz + Pl + Kfs + Bt + Grt ± Sil for samples SCP13, SCP114 and OCP10, and Qz + Pl + Kfs + Bt + Grt + Crd ± Sil for sample SCP106b (Fig. 7h and Table 1). Using the composition of garnet core, convergence of R1, R3 and R4 reactions gives equilibrium average conditions of 795 ± 40 °C and 0.77 ± 0.04 GPa (samples OCP10, SCP13 and SCP114; Fig. 7h and Table 1). Consistently, multi-equilibria P-T estimates (THERMOCALC) yield average temperatures and pressure of 820 ± 45 °C - 0.78 ± 0.06 for the same set of samples (Fig. 7h and Table 1). In the sample SCP106b the Bt-Grt thermometer gives temperatures of 810 ± 20 °C (Fig. 7h and Table 1), whereas Grt-Crd thermometry yields values 35 °C lower (Fig. 7h and Table 1). GBP and GASP barometers estimate average pressures of 0.73 ± 0.07 GPa (Fig. 7 and Table 1). Always, THERMOCALC algorithm produces similar temperatures (800 ± 55 °C; Fig. 7h and Table 1) but higher pressures (0.81 ± 0.07 GPa; Fig. 7h and Table 1) than conventional thermo-barometers. In contrast, when the outermost rim garnet compositions is combined with low-titanium biotite and the lowest anorthite contents in plagioclase, both conventional and multi-equilibria thermobarometry give re-equilibrium P-T conditions between 500 and 600 °C and 0.3–0.5 GPa (Fig. 7h and Table 1).

4.3.3. Schollen-schlieren diatexites

Garnet in schollen-schlieren diatexites also consist in a solid solution dominated by almandine end-member ($Alm_{67-69}Py_{25-27}Grs_{3-4}Sps_{2-3}$), and displays a wide core zone typical of high-temperature diffusion processes (Fig. 8a). However, most garnet shows a slight increase of almandine (X_{Alm} = 0.73–0.74) and decrease of pyrope (X_{Pyp} = 0.20–0.21) towards the outermost rim (Fig. 8a). Biotite has variable X_{Mg} (~0.51–0.57), high Ti contents (0.22–0.30 a. f.u.), and little variation in Al^{IV} (1.26–1.34 a. f.u) and Al^{VI} (0.26–0.37 a. f.u.; Fig. 8c–f). Plagioclase varies between oligoclase and andesine but over narrow compositional range ($Ab_{67-71}An_{28-31}Or_{1-3}$; Fig. 8g). Alkali feldspar is orthoclase with compositions of $Ab_{8-15}An_1Or_{85-92}$ (Fig. 8g), and abundant perthitic intergrowth of intermediate compositions ($Ab_{70-68}An_{12-16}Or_{15-18}$; Fig. 8g).

P-T estimates for the samples SCP18 and OCP14 used the garnet compositions from a wide core zone considering the Qz + Pl + Kfs + Bt + Grt ± Sil mineral assemblage (Fig. 8h and Table 1). Most of the thermo-barometers such as reactions R1, R3 and R4 yield average temperatures and pressures of 835 ± 45 °C - 0.71 ± 0.05 GPa (Fig. 8h and Table 1). Consistently, multi-equilibria calculation (THERMOCALC) gives very similar temperatures and lightly higher pressures (Fig. 8h and Table 1).

4.3.4. Nebulite diatexites

Similarly to the other migmatic rocks, garnet is a solid solution in which predominates almandine over the other end-members. Garnet shows a typical flat zoning pattern with almost constant compositions ($Alm_{66-69}Py_{25-29}Grs_{2-3}Sps_2$; Fig. 9a). Sporadically, a few garnets exhibit narrow compositional variation restricted to external rims suggesting border re-equilibrium driven by Fe–Mg exchange. In these cases, the almandine molar fraction increases to 0.73, with decreasing pyrope molar fraction up to 0.22 (Fig. 9a). Biotite is Ti-rich (0.22–0.29 a. f.u.), has variable X_{Mg} (0.56–0.62), and tetrahedral and octahedral aluminium contents ranging between 1.25 and 1.32 a. f.u. and 0.24–0.32 a. f.u., respectively (Fig. 9b–f). Plagioclase is oligoclase ($Ab_{68-73}An_{26-30}Or_{1-2}$; Fig. 9g) in sample CCP15, and andesine ($Ab_{64-67}An_{32-35}Or_{1-2}$; Fig. 9g) in sample CCP12. Alkali feldspar is orthoclase ($Ab_{10-13}An_1Or_{85-87}$; Fig. 9g) and usually develops perthitic intergrowths of intermediate

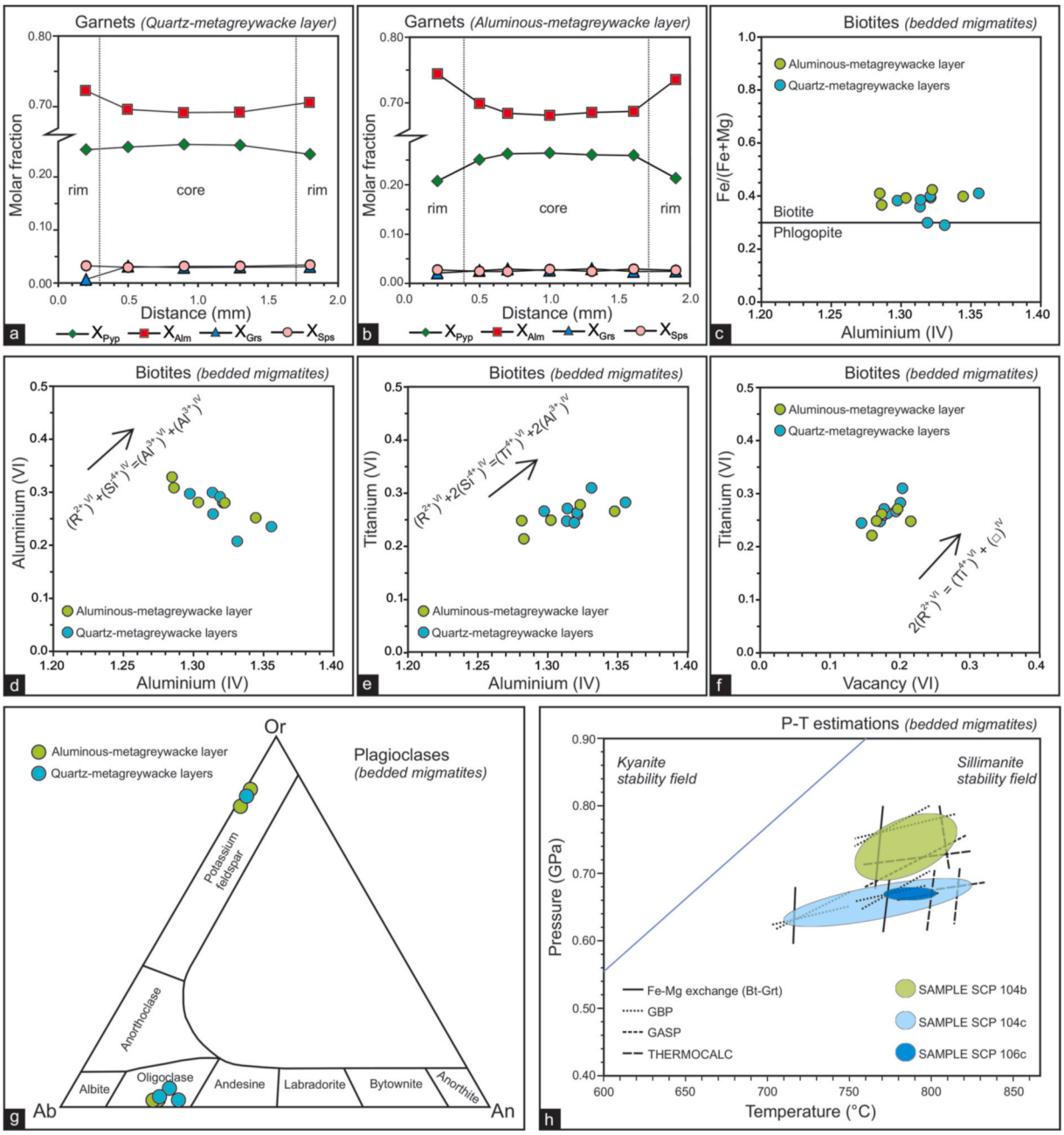

Fig. 6. Mineral chemistry of stromatic metatexites preserving the compositional banding inherited from relict S_0 primary bedding termed as bedded metatexites in Otamendi et al. (2019). a) Compositional garnet profile of quartz-metagreywacke layers. b) Compositional garnet profile of aluminous-metagreywacke layers. c) Classification of micas taken after Deer et al. (1993). d) Aluminium (IV) vs. Aluminium (VI), e) Aluminium (IV) vs. Titanium (VI), and f) Vacancy (VI) vs. Titanium (VI) diagrams. The arrow indicates the direction of ion-exchange vector. g) Anorthite-Albite-Orthoclase ternary diagram. h) P-T diagram showing the equilibrium P-T estimates using core garnet compositions of quartz-metagreywacke and aluminous-metagreywacke layers.

compositions ($Ab_{30-45}An_{3-8}Or_{46-65}$; Fig. 9g). Irrespective of the textural position, cordierite has uniform X_{Mg} (~0.73–0.74).

Conventional thermobarometric estimates for nebulite diatexites (i.e., samples CCP12 and CCP15) was performed using the mineral assemblage Qz + Pl + Kfs + Bt + Grt + Crd + Sil (Fig. 9h and Table 1). For garnet core compositions, the R1 and R2 thermometers yield similar equilibrium temperatures around 755 ± 45 °C (Fe–Mg exchange Grt-Bt) and 780 ± 35 °C (Fe–Mg exchange Grt-Crd) in the sample CCP12 (Fig. 9h and Table 1); and between 805 ± 30 °C (Fe–Mg exchange Grt-Bt) and 785 ± 30 °C (Fe–Mg exchange Grt-Crd) for the sample CCP15 (Fig. 9h and Table 1). In contrast, equilibrium pressures range between ~0.55 and 0.7 GPa (Fig. 9h and Table 1). Supporting conventional thermobarometry, similar P-T conditions of 855 ± 55 °C - 0.66 ± 0.1 GPa (sample CCP12; Fig. 9h and Table 1) and 850 ± 59 °C - 0.67 ± 0.09 GPa (sample CCP15; Fig. 9h and Table 1) are obtained with THERMOCALC.

4.4. U–Pb geochronology

4.4.1. Nebulite diatexite (sample CCP40)

Zircon in this sample has variable morphologies ranging from sub-rounded prisms with irregular or fragmented edges to ovoid crystals. CL images show a homogeneous and concentrically to irregular zoned crystals (Fig. 10a). The U/Pb concordia plot gives the widest age spectrum of the three studied samples (Fig. 10b). The older concordant age (Fig. 10b) is a single spot analyzed in the core of a concentrically zoned

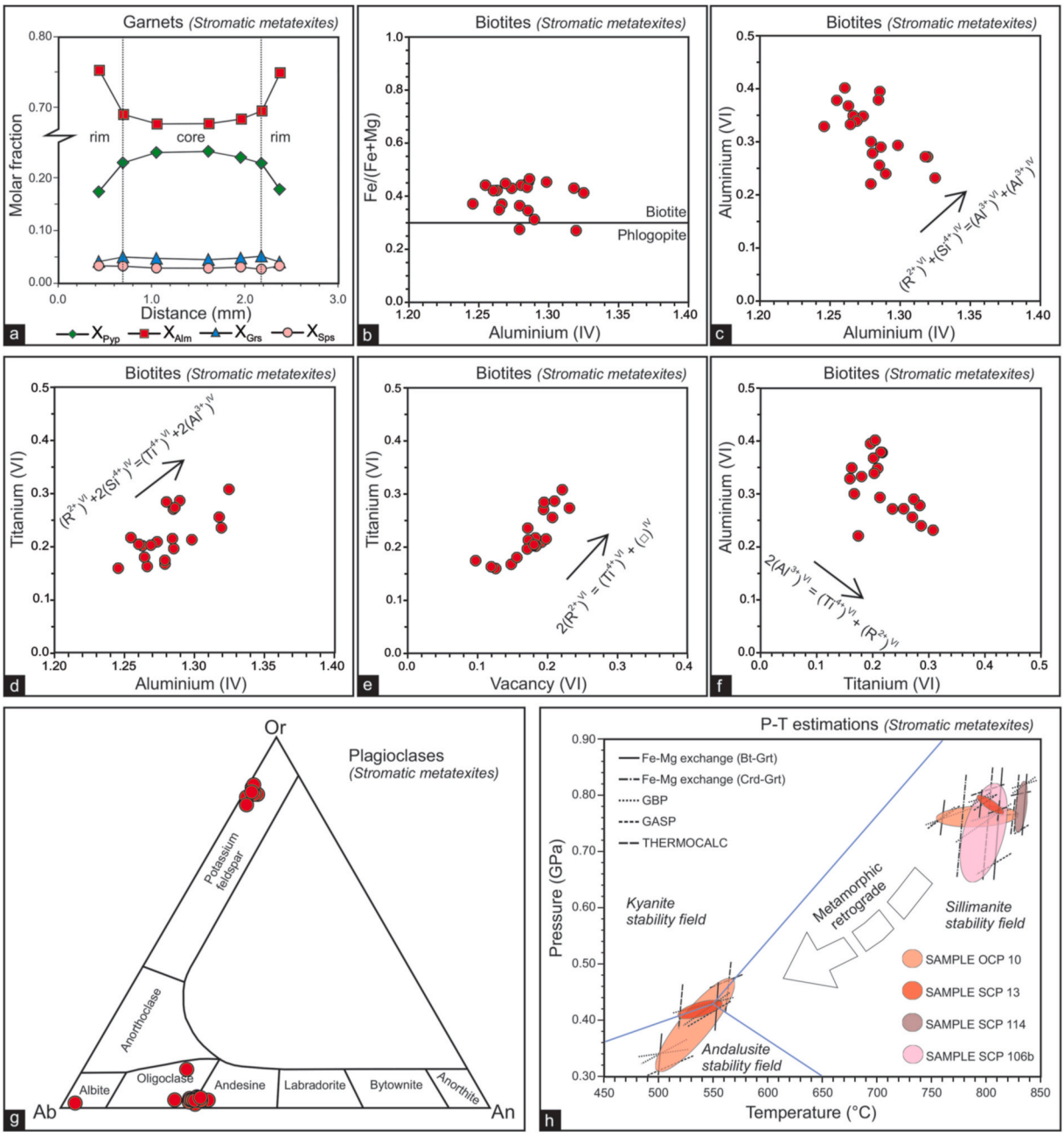

Fig. 7. Mineral chemistry of stromatic metatexites dominated by syn-migmatic fabrics. a) Compositional garnet profile. b) Classification of micas taken after Deer et al. (1993). c) Aluminium (IV) vs. Aluminium (VI), d) Aluminium (IV) vs. Titanium (VI), e) Vacancy (VI) vs. Titanium (VI), and f) Titanium (VI) vs. Aluminium (VI) diagrams. The arrow indicates the direction of ion-exchange vector. g) Anorthite-Albite-Orthoclase ternary diagram. h) P-T diagram showing the metamorphic peak conditions estimated from core garnet compositions, and the retrograde path inferred from rim garnet compositions.

zircon, with Th/U values of 0.98 that yields a $^{207}Pb/^{206}Pb$ age of 1839 Ma. Nonetheless, the two most important age clusters consist in Mesoproterozoic and Neoproterozoic inherit ages. Mesoproterozoic ages, comprising thirteen spots analyzed in the zircons core zone and near core zone with Th/U values between 0.11 and 0.82, show age ranging from 850 to 1182 Ma (Fig. 10b). Whereas, Neoproterozoic ages include fifteen spots with Th/U ranging between 0.12 and 0.77 and two analyses with Th/U < 0.1, measured in near core zone of zircons, that gives ages between 551 and 704 Ma (Fig. 10b). The youngest ages group contains a population of eight spots analyzed in or near the zircons rim (with Th/U values between 0.04 and 0.48) that yields Cambrian ages ranging from 525 to 544 Ma with a Tukey's Biweight Mean of 533.7 ± 5.7 Ma (Fig. 10b and c).

4.4.2. Stromatic metatexite (sample SCP13)

Zircon has irregular to sub-rounded morphologies, and occasionally displays bipyramidal edges. In addition, CL images (Fig. 11a) show an irregular to concentrically zoned core, surrounded by a thin low-luminescence rim. In effect, the rim zone, often considered to record the last stage of metamorphic recrystallization, is commonly less thick than the laser ablation spot (≥30 μm). Therefore, analysis for this specimen focused mainly on retrieving inherited ages. The Th/U values in the zircons core zone generally vary between 0.15 and 0.7, which is commonly associated with igneous zircons (Hoskin and Schaltegger, 2003). Projection on Concordia plot yields concordant ages with a polymodal distribution in a range between 1837 and 597 Ma (Fig. 11b and c). The two most important age peaks display a bimodal distribution and

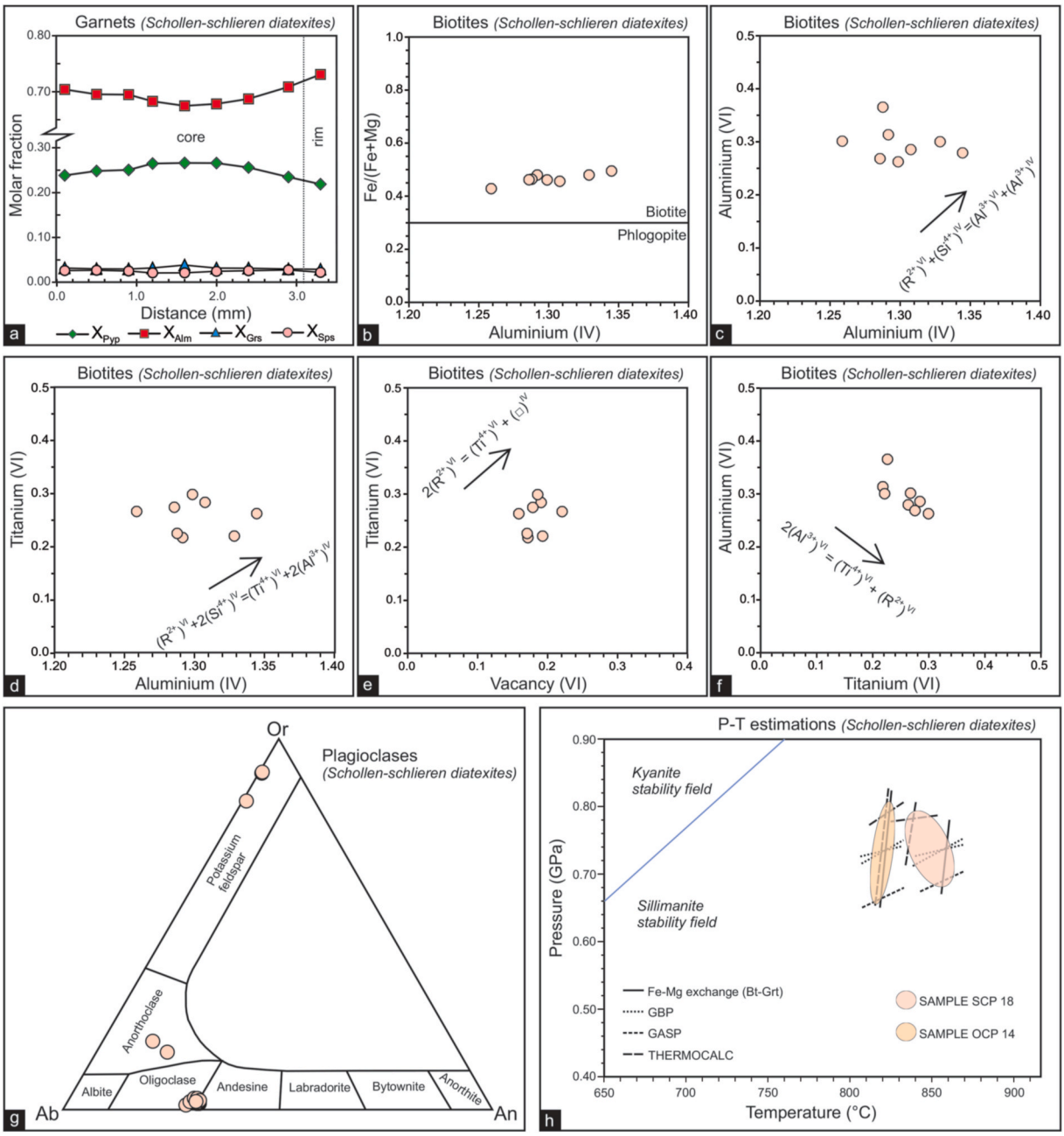

Fig. 8. Mineral chemistry of schollen-schlieren diatexites. a) Compositional garnet profile. b) Classification of micas taken after Deer et al. (1993). c) Aluminium (IV) vs. Aluminium (VI), d) Aluminium (IV) vs. Titanium (VI), e) Vacancy (VI) vs. Titanium (VI), and f) Titanium (VI) vs. Aluminium (VI) diagrams. The arrow indicates the direction of ion-exchange vector. g) Anorthite-Albite-Orthoclase ternary diagram. h) P-T diagram showing the metamorphic peak conditions determined from core garnet compositions.

widely overlap with Mesoproterozoic and Neoproterozoic age clusters of sample CCP40. The young age cluster of seventeen spot data has ages ranging between 597 and 734 Ma (Neoproterozoic; Fig. 11c), whereas the old age cluster includes sixteen analyses spreading between 900 and 1116 Ma (Mesoproterozoic; Fig. 11c). Subordinately in the amount of data, a third peak of four spots data yields Paleoproterozoic ages between 1751 and 1837 Ma (Fig. 11c), which is coincident with older concordant age of sample CCP40. The entire data of zircon ages yields two isolated concordant ages of 1658 and 831 Ma, which are concordant but unrelated to other data.

4.4.3. *Schollen-schlieren diatexite (sample SCP527)*

Zircon has prismatic shape and usually develops bipyramidal faces. CL images (Fig. 12a) display both homogeneous and zoned crystals, which may have a thin rim of low luminescence. The Th/U values measures in the rim to near core zone range between 0.05 and 0.51, although one single spot have Th/U of 0.84. These Th/U ratios could suggest either igneous crystallization, metamorphic growth or a combination of both (Yakymchuk et al., 2018). The U/Pb concordia projection shows three main ages groups (Fig. 12b). One age cluster includes seventeen analyses with ages ranging from 566 to 556 Ma (Fig. 12b) that partially matches with the youngest Neoproterozoic ages of sample CCP40. A second cluster, which includes twenty-six analyses, yields ages ranging between 544 and 532 Ma with a weighted average $^{206}Pb/^{238}U$ age of 538.7 ± 5.3 Ma (Fig. 12b and c). This age cluster is broadly concordant with the Cambrian ages registered in the sample

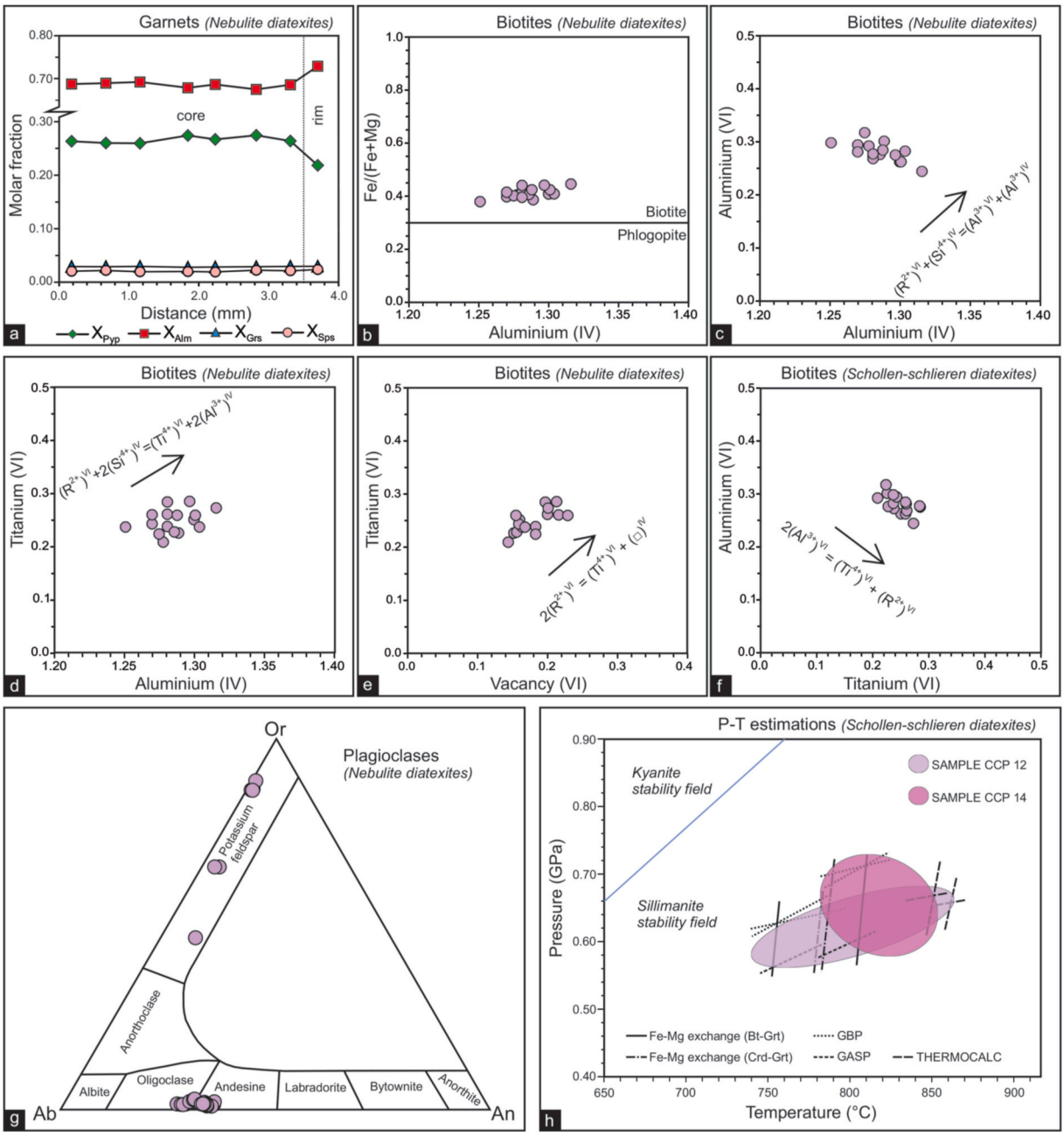

Fig. 9. Mineral chemistry of nebulite diatexites. a) Compositional garnet profile. b) Classification of micas taken after Deer et al. (1993). c) Aluminium (IV) vs. Aluminium (VI), d) Aluminium (IV) vs. Titanium (VI), e) Vacancy (VI) vs. Titanium (VI), and f) Vacancy (VI) vs. Aluminium (VI) diagrams. The arrow indicates the direction of ion-exchange vector. g) Anorthite-Albite-Orthoclase ternary diagram. h) P-T diagram showing the equilibrium conditions calculated from core garnet compositions.

CCP40. A third age cluster is less representative and only consists of four analyses with ages ranging between 511 and 508 Ma (Fig. 12b).

5. Discussion

5.1. Thermobarometry and P-T path reconstruction

P-T estimates of representative migmatites usually represent only some segment of the P-T path followed by a bulk crustal section (Bucher and Grapes, 2011). Yet, combining segments of P-T paths retrieved in individual specimens of a metamorphic sequence, allows recognizing common petrological processes and discussing whether the metamorphic history corresponds to a single-cycle or multi-step tectono-thermal evolution. In the study area, thermobarometry enables recognizing five transient stages of mineral equilibrium. Collectively, these five steps define the P-T path of the entire metamorphic sequence (Fig. 13).

Garnet cores of the patch and net metatexites (sample SCP301) preserve the oldest metamorphic stage (Fig. 13), as the refractory garnet core composition records prograde metamorphism under sub-solid conditions. The presence of low-Ti biotite laths inside garnet cores, associated with the paleosome mineral assemblage, reflects that the earliest preserved metamorphic stage reached a narrow temperature range (620–650 °C; Table 1). In contrast, the lack of both plagioclase and alumina polymorph as inclusion in garnet cores introduces a large uncertainty in barometric calculations. Instead, the presence of relict

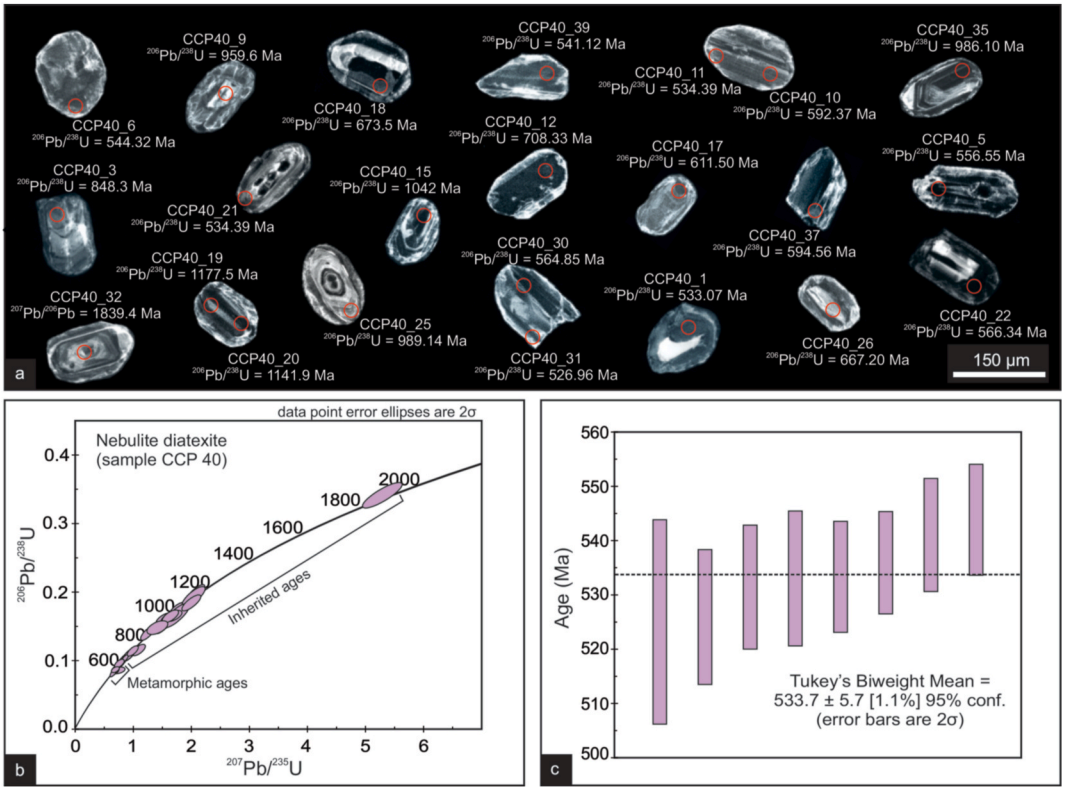

Fig. 10. a) a) Cathodoluminescence images of zircon analysis in a nebulite diatexite (sample CCP40). b) Conventional U–Pb concordia diagram showing the inherited and metamorphic ages. c) Tukey's Biweight Mean for metamorphic ages.

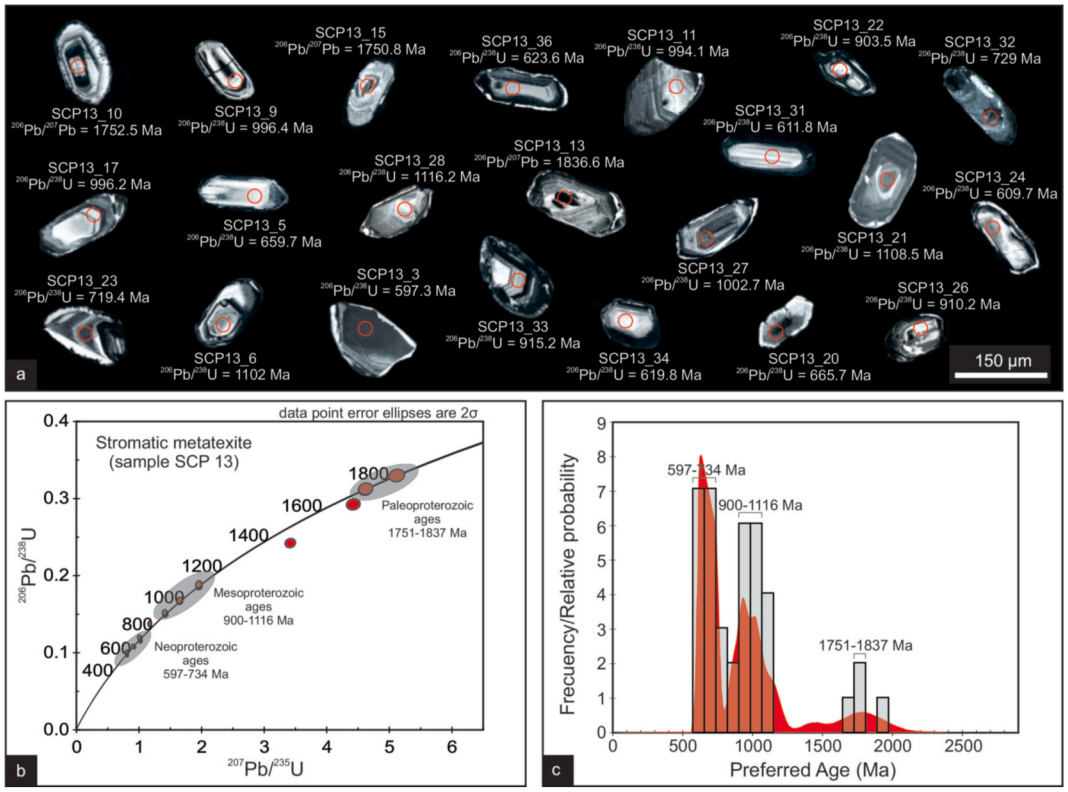

Fig. 11. Cathodoluminescence images of zircon analysis in a stromatic metatexite (sample SCP13). b) Conventional U–Pb concordia diagram. Grey ellipses indicate the dominant clusters of inherited ages. c) Probability density plot diagram showing the age pattern of detrital zircons in which are marked the three principal age peaks.

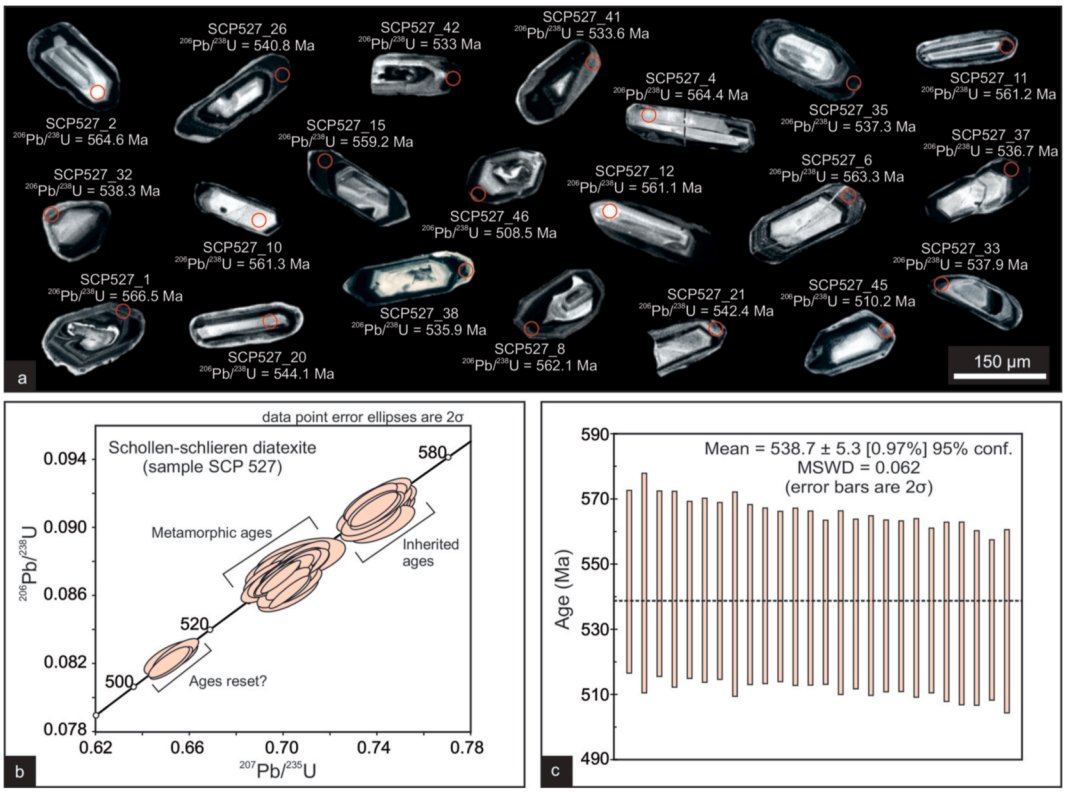

Fig. 12. a) Cathodoluminescence images of zircon analysis in a schollen-schlieren diatexite (sample SCP527). b) Conventional U–Pb concordia diagram showing the distribution of inherited, metamorphic, and resetting ages. c) Weighted average $^{206}Pb/^{238}U$ age for metamorphic ages.

kyanite shows a metamorphic path evolving through the kyanite stability field before anatexis. It should be noted that metastable preservation of kyanite is well known in migmatites from nearby granulite-facies metamorphic sections (Guereschi and Martino, 2014). In the study area, the kyanite stability field spans a large pressure range between 0.69 and 0.83 GPa at the temperature retrieved from biotite included in garnet cores (Table 1).

A second transient equilibrium stage is recorded in stromatic metatexites that conserve the compositional banding inherited from relict S_0 primary bedding (quartz-metagreywacke and aluminous-metagraywacke layers; Fig. 13). Whole-rock chemistry data and petrogenetic models showed that each migmatic layer retains a bulk composition closely unmodified regarding its original metasedimentary precursors (Barzola et al., 2019a; Otamendi et al., 2019). An average temperature and pressure estimated for both an aluminous-metagreywacke metamorphic rock (i.e., sample SCP104b) and quartz-metagreywacke rocks (i.e., samples SCP104c and SCP106c) bracket the onset of partial melting at 770 ± 60 °C and 0.72 ± 0.05 GPa (Fig. 13; Table 1). This result concurs with experimental petrology that studied dehydration melting of pelites and greywackes under the P-T condition of interest (Clemens and Vielzeuf, 1987; Patiño Douce and Beard, 1995; Montel and Vielzeuf, 1997).

The third equilibrium condition recorded in the studied migmatites is widespread preserved, and corresponds to both temperature and pressure reached at the metamorphic peak (Fig. 13). Stromatic metatexites with pre-migmatitic structures entirely obliterated by anatexis (samples OCP10, SCP13, SCP114, and SCP106b) unraveled metamorphic peak at 800 ± 50 °C and 0.78 ± 0.05 GPa (Table 1). Similar P-T conditions are retrieved in garnet rim compositions of the patch and net metatexite (sample SCP301) and schollen-schlieren diatexites (samples SCP18 and OCP14). In particular, schollen-schlieren diatexites record average P-T conditions of about 830 ± 55 °C and 0.75 ± 0.08 GPa (Table 1). Consequently, the most reliable estimates reflect that temperatures rose to 815 ± 60 °C at middle crustal pressures of ~0.77 ± 0.06 GPa during the metamorphic peak. Several previous studies in the Sierras de Córdoba reached similar results; for this reason, there is a consensus that the metamorphic peak attained granulite-facies temperatures of 700–850 °C at pressures of about 0.65–0.85 GPa (Gordillo, 1984; Martino et al., 1994; Baldo et al., 1996; Rapela et al., 1998; Otamendi et al., 1999, 2004, 2004; Guereschi and Martino, 2008, 2014, 2014; Barzola et al., 2019a).

A fourth P-T stage is preserved in nebulite diatexites (samples CCP12 and CCP15) which record average temperatures of 805 ± 60 °C (Fig. 13, Table 1). However, an estimated average pressure of ~0.64 ± 0.09 GPa for nebulite diatexites is ~0.1 GPa lower than the barometric peak inferred for stage 3, suggesting relatively rapid decompression in an essentially isothermal system. Estimated pressures for the stage 4 are almost identical to the late decompression stage in granulite-facies metamorphic rocks of the Calamuchita Metamorphic Complex, reflecting that before starting to cool down the metamorphic rocks underwent a decompression of at least 0.15 GPa (Otamendi et al., 2004). In the same line, our argument agrees with average equilibrium pressures (0.65 ± 0.05 GPa) postulated by Gordillo (1984) for Cerro Pelado massif.

A last recorded P-T condition is retained in garnet rim compositions of some stromatic metatexites (samples SCP13 and OCP10). The last stage occurred at temperatures and pressures between 500 and 600 °C and 0.3–0.5 GPa, respectively (Table 1). Most likely, however, the cooling event was related to retrograde metamorphism of migmatic sequence (Fig. 13). These results are similar to P-T estimates for the roof block of the Guacha Corral Shear Zone, located immediately west of the study area (Martino, 2003; Whitmeyer and Simpson, 2003; Otamendi et al., 2004; Semenov and Weinberg, 2017), and with the cooling rate of 9 °C/Ma calculated by Steenken et al. (2010) for the boundaries of Sierras de Córdoba.

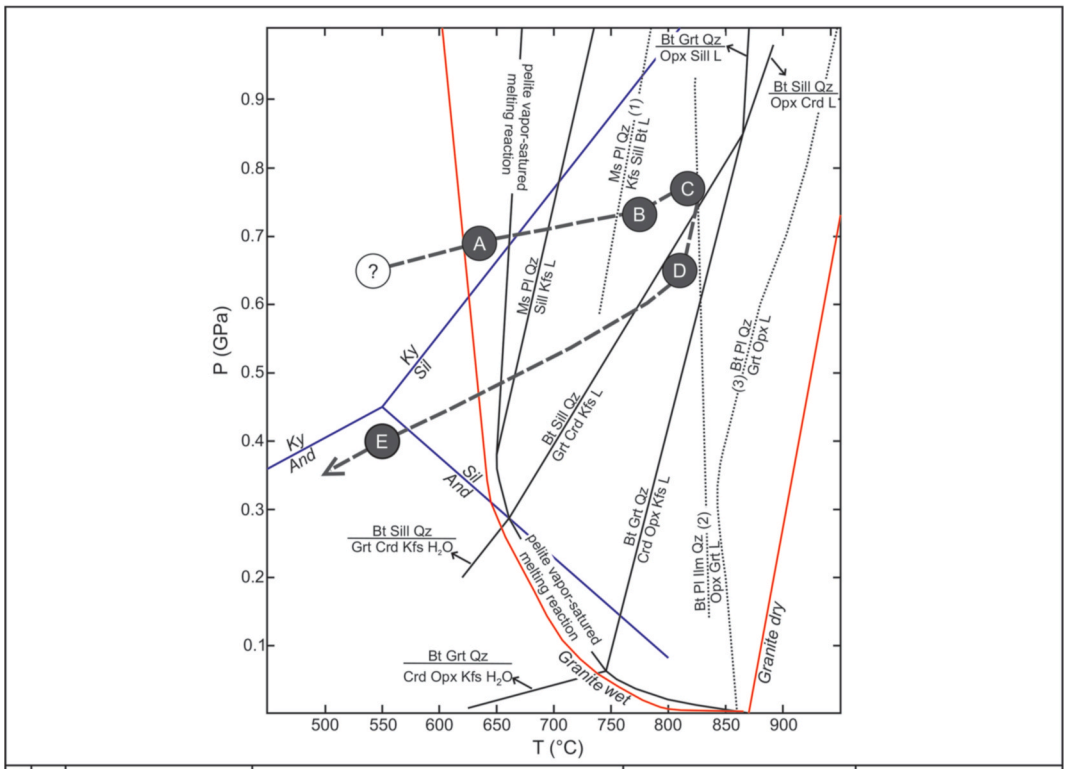

Period time	P-T point	Petrogenetic process	Textural and morphological features	Structural features	Age
Ordovician	E	Retrograde metamorphism T = 500-600 °C P = 0.3-0.5 GPa	Low-T deformed migmatites (protomylonites to mylonites) Mineral assemblage: Qz+Pl+Bt+Ms±Chl	S_3 mylonitc foliation	~ 486-470 Ma (Steenken et al., 2010; Demartis et al., 2017; Semenov et al., 2019)
Cambrian	D	Emplacement of anatectic granitoids and isothermal exhumation T = 805 ± 60 °C P = 0.64 ± 0.09 GPa	High-T deformed migmatites Mineral assemblage:Qz+Pl+Kfs+Bt+Grt±Fi Nebulite diatexite Mineral assemblage: Qz+Pl+Kfs+Bt+Grt+Crd±Sil	S_{2c} high-temperature shear band S_{2b} axial plane foliation	~ 540 - 525 Ma (Rapela et al., 1998; Sims et al., 1998; Escayola et al., 2007; Tibaldi et al., 2008, 2019; Siegesmund et al., 2010; Murra et al., 2016; D'Eramo et al., 2020; this work)
	C	Migmatic system peak T = 815 ± 60 °C P = 0.77 ± 0.06 GPa	Schollen-schlieren diatexites Mineral assemblage: Qz+Pl+Kfs+Bt+Grt±Sil±Crd Stromatitc migmatites (obliterated pre-migmatitic structures) Mineral assemblage: Qz+Pl+Kfs+Bt+Grt±Sil±Crd	S_{2a} + F_2 folded stromatic foliation *(F_2 = heterogeneous fold system)*	Progressive non-coaxial and compressive deformation
	B	Onset partial melting T = 760 ± 60 °C P = 0.72 ± 0.05 GPa	Stromatic migmatites (preserved pre-migmatitic structures) Mineral assemblage: Qz+Pl+Bt+Grt±Kfs±Sil	S_{2a} stromatic foliation	
Neoproterozoic	A	Early metamorphism T = 620-650 °C P = 0.69-0.78 GPa	Aluminous- to quartz-metagreywaques Mineral assemblage: Qz+Pl+Bt±Grt	S_1 sub-solid metamorphic foliation	Gneiss Las Palmas 543 ± 4 Ma (Siegesmund et al., 2010)
		Sedimentation of migmatic precursors	Aluminous to quartz greywaques sediments	S_0 relict primary bedding	Maximum depositional age ca. 560-550 Ma (Sims et al., 1998; Iannizzotto et al., 2013; this work)

Fig. 13. P-T diagram illustrating the pressure-temperature path retrieved through thermobarometry of the anatectic rocks. A synopsis of the metamorphic evolution is show below as inset box. The P-T stability of alumina polymorphs in the P-T space is after Pattison (1992). Water-saturated (wet) and dehydration melting (dry) for muscovite granite (red lines) are after Thompson (1996). Metamorphic reactions (bold lines) are from P-T grid in NaKFMASH system after Spear et al. (1999), and partial melting reactions (dashed lines) are from source data of: (1) Patiño Douce and Harris (1998), (2) Patiño Douce and Beard (1996), and (3) Vielzeuf and Montel (1994). Mineral symbols are after Whitney and Evans (2010), H_2O = water, L = melt. (For interpretation of the references to colour in this figure legend, the reader is referred to the Web version of this article.)

5.2. *Significance of the U–Pb geochronology*

5.2.1. *Detrital zircon (DZ) and maximum depositional age (MDA)*

Detrital zircon geochronology is a powerful tool to constrain the depositional age of sediments, reconstruct provenance pathways, and correlate different lithological sequences (Gehrels, 2014 and references therein). During the past two decades, detrital zircon data have been used to correlate metasedimentary sequence from central and north-western Argentina (Rapela et al., 1998, 2007, 2016, 2007; Schwartz and Gromet, 2004; Escayola et al., 2007; Adams et al., 2008, 2010, 2010; Casquet et al., 2018; Perón Orrillo et al., 2019). In particular, an emphasis was on testing the temporal relationships among the very

low-grade sediments of Puncoviscana Formation in northwestern Argentina and the high-grade metasedimentary sequences that extend at least to the Sierras de Córdoba.

This work presents three new U/Pb zircon ages (specimens SCP13, SCP527, and CCP40) for the granulite-facies metasedimentary rocks from the western Pampean orogenic belt. A common feature of these samples is the prevailing presence of inherited zircon ages. Zircon age patterns yield a contribution of Neoproterozoic (551–734 Ma) and Mesoproterozoic (850–1182 Ma) zircons and minor proportions of Paleoproterozoic zircon grains (1751–1839 Ma), which are similar to those recorded in other sectors of the Sierras Pampeanas (Rapela et al., 1998, 2007; Sims et al., 1998; Pankhurst et al., 2000; Schwartz and Gromet, 2004; Escayola et al., 2007; Collo et al., 2009; Drobe et al., 2011; Verdecchia et al., 2011; Cristofolini et al., 2012; Perón Orillo et al., 2019; among others).

Detrital zircon ages are relevant for constraining the maximum depositional age (MDA) of sedimentary precursors of the migmatic sequence. The youngest single grain (Dickinson and Gehrels, 2009) analyzed for stromatic metatexite (sample SCP13) gives a MDA of 597 ± 5.3 Ma. Detrital ages of 588 ± 32 Ma in the Tuclame schists (Schwartz and Gromet, 2004) and 585 ± 16 Ma in the Quilpo Formation (Sims et al., 1998), in the northern region of the Sierra de Córdoba, are consistent with the youngest single grain measure in the stromatic metatexite SCP13. Nevertheless, the youngest grain cluster at 2σ provides a most reliable MDA (Dickinson and Gehrels, 2009; Coutts et al., 2019). Thus, diatexites SCP527 and CCP40 yield a MDA of 557.8 ± 3 Ma and 552.3 ± 3.8, respectively, suggesting that the sedimentation process was active, at least, until 560-550 Ma. This interpretation agrees with the maximum depositional age of 561 ± 10 Ma reported in migmatitic gneisses from the Pichanas Complex (Sims et al., 1998). A similar conclusion reached Iannizzotto et al. (2013) in gneisses from Sierra Norte de Córdoba, where the youngest inherited peak is around ~ 560 Ma. Based on the literature and new data, we propose that the maximum depositional age of the sedimentary precursors in the study area occurred during the Ediacaran (ca. 560-550 Ma). This result concurs with a recent interpretation (Baldo et al., 2014) that integrated detrital ages from the literature (Escayola et al., 2007; Drobe et al., 2011) to show that the depositional ages of migmatite sedimentary progenitors from the Sierras de Córdoba spanned over the range between 570 and 541 Ma.

5.2.2. Zircon growth during granulite-facies metamorphism and anatexis

The new U/Pb zircon ages measured in schollen-schlieren (sample SCP527) and nebulite (sample CCP40) diatexites are consistent with high-grade metamorphism and anatexis linked to the Pampean Orogeny (Ramos, 1988; Rapela et al., 1998). The oldest age of the Pampean metamorphism is at about 543 ± 4 Ma as it is conserved in the gneiss Las Palmas (Siegesmund et al., 2010), which shortly post-dates our proposed maximum depositional age for the metasedimentary rocks (ca. 560-550 Ma). Over the studied area, the metamorphic peak and anatexis begun at ~540 Ma and it is recorded by the metamorphic ages of 538.7 ± 5.3 Ma (specimen SCP527) and 533.7 ± 5.7 Ma (specimen CCP40). The metamorphic climax may have endured, at least, until 520 Ma since numerous U/Pb ages in zircons and monazites taken from anatectic granitoids range between 535 and 520 Ma (Rapela et al., 1998; Sims et al., 1998; Gromet and Simpson, 1999; Tibaldi et al., 2008, 2019; Ramos et al., 2015; Murra et al., 2016; D'Eramo et al., 2020). The relatively younger ages registered in zircon rims of the schollen-schlieren diatexite of around 511 Ma and 508 Ma perhaps represent metamorphic overprint due to isotopic re-equilibration during cooling and re-hydration (Siegesmund et al., 2010).

5.3. Metamorphic evolution and migmatization

A metamorphic event constitutes a tectono-thermal episode encompassing prograde, peak, and retrograde segments (see Spear, 1993; Vernon et al., 2008 for comprehensive treatment of metamorphic evolution). The entire metamorphic evolution is possibly linked to several generations of folds and/or foliations, and involves a complex mineral reaction history defined by progressive changes in the stable mineral assemblages along the P–T path.

Within the study area, the prograde metamorphic path is poorly preserved, and only locally relicts of pre-migmatitic structures and mineral assemblages provide evidence for reconstructing the history before anatexis. In this sense, vestiges of the sedimentary process are preserved as a relict S_0 primary bedding. Petrographic and textural analysis, added to previous whole-rock chemistry studies, suggest that these precursors derived mainly from aluminous-to quartz-greywackes (Otamendi and Patiño Douce, 2001; Barzola et al., 2019a; Otamendi et al., 2019). In this regard, the new detrital zircons ages support an ending of sedimentary deposition at the Ediacaran (ca. 560-550 Ma; Fig. 13).

Petrographic analyses and structural evidence added to the new thermobarometry data suggests that the sedimentary sequence underwent an early metamorphic stage, probably linked with the evolution of an accretionary prism adjacent at the Pampean magmatic arc (Northrup et al., 1998; Simpson et al., 2003; Schwartz et al., 2008; Von Gosen and Prozzi, 2010; Von Gosen et al., 2014), and recorded thickening of Pampean orogenic crust (Otamendi et al., 2004). The early metamorphism is characterized by the development of S_1 sub-solid foliation, preserved in paleosomes and refractory layers of migmatites, and P-T conditions restricted to temperatures of 620–650 °C within the kyanite stability field (0.69–0.78 GPa; Fig. 13). A metamorphic age of 543 ± 4 Ma in the garnet-rich gneiss of Las Palmas (Siegesmund et al., 2010) may be associated with this stage of the prograde P-T path.

The first record of anatexis in the metasedimentary sequence is given by the generation of metatexites that developed an S_{2a} stromatic foliation but still preserve pre-migmatitic structures such as compositional banding inherited from relict primary bedding. The equilibrium conditions observed in quartz- and aluminous-metagreywackes layers restrict the onset of partial melting at average temperatures and pressures of 770 ± 60 °C and 0.72 ± 0.05 GPa (Fig. 13). Petrographic and textural features point at the occurrence of K-feldspars in the mineral assemblage marks the beginning and progress of the partial melting process (Gordillo, 1984; Otamendi et al., 1999; Guereschi and Martino, 2008, 2014, 2014; Barzola et al., 2019a). For this reason, aluminous-metagreywackes layers display a large volume fraction of leucosomes, wherein K-feldspars occurs in higher proportions than in quartz-metagreywackes layers. A positive correlation between the K-feldspar modal fraction and in-situ leucosomes was taken to reflect that anatexis was diachronic and its stability was mainly controlled by protolith composition (Tibaldi et al., 2019).

The progress of partial melting was a continuous process by which pre-migmatitic structures were progressively replaced by a set of syn-migmatitic structures during a non-coaxial compressive deformation. S_{2a} stromatic foliation was affected by a heterogeneous fold system (F_2), and the progressive tightening led to the generation of S_{2b} axial plane foliation. Leucosomes and anatectic granitoids emplaced along S_{2a} and S_{2b} structures do not display textural, mineralogical, and chemistry differences suggesting that they constituted a network of interconnected melts that formed migration channels (Barzola et al., 2019b; Otamendi et al., 2019; Tibaldi et al., 2019). The channelized melt-flow became self-reorganized through extraction/accumulation processes, as deformation was partitioned into lower and higher strain zones (Brown, 1994, 2007, 2007; Sawyer, 1994, 2001, 2001; Brown and Solar, 1998; Lee et al., 2018). Along lower-strain domains, $S_{2a} + F_2$ folded stromatic foliations dominate, whereas in high-strain zones S_{2b} axial plane foliation or, locally, S_{2c} high-temperature (amphibolite/granulite-facies) shear foliation are predominant. Furthermore, melt self-reorganization strongly controlled the distribution pattern of diatexite rocks. Melt drained from forelimbs to hinges in F_2 folds promoted melt accumulation and dismembered of stromatic structure generating

schollen-schlieren diatexites. Instead, S_{2b} structures worked as main melts flow-channels and probably favored to emplacement of nebulite diatexite at relatively shallow cortical levels. However, it cannot be completely ruled out that non-coaxial deformation has been accommodated at the end-stage by local extensional shear zones, which helped with melt extraction and juxtaposed metatexite rocks with nebulite diatexite (Otamendi et al., 2004). Extensional shear zones have been recognized inside of Calamuchita Metamorphic Complex and described as coeval with the thrusting and shortening (Otamendi et al., 2004). Over the Calamuchita Metamorphic Complex, extensional shearing was likely also coeval with local development of S_{2c} high-temperature shear foliation. In such a case, these shear zones could have favored orogenic exhumation during and/or immediately after the metamorphic peak. Based on the mineralogical, textural, and thermobarometric evidence presented in this work, the exhumation process was relatively rapid and essentially isothermal, which is consistent with the metamorphic trajectory reconstructed by Otamendi et al. (2004).

Structural observations are supported by the new P-T estimates and geochronology data presented here. Metatexites and schollen-schlieren diatexites preserve peak conditions of migmatization (815 ± 60 °C and 0.77 ± 0.06 GPa; Fig. 13). In contrast, nebulite diatexites were stabilized at similar temperature but slightly lower pressure (805 ± 60 °C and 0.64 ± 0.09 GPa; Fig. 13) than metatexites and schollen-schlieren diatexites. Nonetheless, metamorphic ages preserved in diatexitic rocks do not show a substantial time-lag between them. Similar U/Pb zircon age between schollen-schlieren diatexite (538.7 ± 5.3 Ma) and nebulite diatexite (533.7 ± 5.7 Ma) reflects a nearly continuous deformation and partial-melting history. Thus, the petrological, structural, thermobarometric, and geochronological data enable reassessing the development of the different migmatitic rock types. The diversity of migmatites was driven by variable degree of melt accumulation/extraction anatectic process, and it happened during a progressive anatectic event assisted by predominantly compressive non-coaxial deformation (see also Tibaldi et al., 2019).

The final stage of metamorphic evolution is associated to the final exhumation of the metasedimentary sequence from middle (~0.7–0.8 GPa) to middle-shallow (~0.5–0.3 GPa) crustal levels. Uplift is documented by textural and structural reworking. Although the first textural evidence of retrogression is biotite rimming garnets, the clearest feature of tectonic reworking is the development of tight shear bands with S_3 mylonitic foliation and the replacement of the migmatic mineral assemblage by the muscovite + chlorite association. P-T estimates restrict the retrograde stage to temperatures of 500–600 °C and pressures between 0.3 and 0.5 GPa (Fig. 13) as already observed in the hanging wall of the Guacha Corral Shear Zone (Martino, 2003; Whitmeyer and Simpson, 2003; Otamendi et al., 2004; Semenov and Weinberg, 2017; Semenov et al., 2019).

6. Conclusion

Based on the petrographic analyses, structural observation, thermobarometric estimates, and U/Pb zircon geochronology we propose that widespread anatexis was a diachronic and progressive event associated with the Pampean Orogeny. P-T-*t* path shows a clockwise evolution. The prograde path evolved from amphibolite-facies (620–650 °C) through kyanite stability field (0.69–0.78 GPa) to the granulite-facies in the sillimanite stability field. The metamorphic peak reached temperatures higher than 800 °C at middle crustal levels (0.77 ± 0.06 GPa). Nebulite diatexites record slightly lower pressures (0.64 ± 0.09 GPa) but similar peak temperatures (805 ± 60 °C), suggesting melt extraction and isothermal uplifted of the metamorphic section. U/Pb zircon geochronology shows that granulite-facies metamorphism, and anatexis lasted at least 15 Ma (~540-525 Ma). The retrograde path evolved from low-amphibolite- to greenschist-facies (500–600 °C and 0.3–0.5 GPa) and is locally recorded in narrow shear bands. The P-T-*t* path developed coeval with a predominantly compressive non-coaxial deformation. The different migmatitic rock types are syn-deformational lithological products linked to melting self-reorganization (extraction/accumulation processes) within the migmatitic massif itself, and only in subordinate way to variation in the protolith compositions or the peak metamorphic condition.

Credit author statement

All the authors of this paper worked in research, conceptualization, data analysis, methodologies, writing and editing.

Declaration of competing interest

The authors declare that they have no known competing financial interests or personal relationships that could have appeared to influence the work reported in this paper.

Acknowledgment

We acknowledge Professor Pablo D. González and an anonymous reviewer for helpful and thoughtful reviews which improved the manuscript. This work was funded by ANPCYT-Argentina through grants PICT 2549/17 and PICT 296/17, SeCyT-UNRC grant PIP 18/C485 and PIP 18/C573. Argentinean researchers were supported by Consejo Nacional de Investigaciones Científicas y Técnicas, Argentina and Universidad Nacional de Río Cuarto. We thank Zhan Peng for assistance with U–Pb zircon geochronology at California State University Northridge.

Appendix A. Supplementary data

Supplementary data to this article can be found online at https://doi.org/10.1016/j.jsames.2021.103534.

References

Adams, C., Miller, H., Toselli, A.J., Griffin, W., 2008. The Puncoviscana Formation of northwest Argentina: U-Pb geochronology of detrital zircons and Rb-Sr metamorphic ages and their bearing on its stratigraphic age, sediment provenance and tectonic setting. Neues Jahrbuch Geol. Palaontol. Abhand. 247, 341–352.

Adams, C., Miller, H., Aceñolaza, G., Toselli, A., Griffin, W., 2010. The Pacific Gondwana margin in the late Neoproterozoic-early Paleozoic: detrital zircon U-Pb ages from metasediments in northwest Argentina reveal their maximum age, provenance and tectonic setting. Gondwana Res. 19, 71–83.

Baldo, E., Demange, M., Martino, R., 1996. Evolution of the Sierras de Córdoba, Argentina. Tectonophysics 267, 121–142.

Baldo, E., Rapela, C., Pankhurst, R., Galindo, C., Casquet, C., Verdecchia, S., Murra, J., 2014. Geocronología de las Sierras de Córdoba: revisión y comentarios. In: Martino, R., Guereschi, A. (Eds.), Geología y Recursos Naturales de la Provincia de Córdoba, Relatorio del 19° Congreso Geológico Argentino, Córdoba, pp. 845–868.

Barzola, M., Tibaldi, A., Otamendi, J., Cristofolini, E., Demichelis, A., Armas, P., Camilletti, G., 2019a. Geología del basamento del sector sur del Embalse Cerro Pelado, Sierra de Comechingones, Córdoba: análisis geotermobarométrico de las rocas anatécticas. Rev. Asoc. Geol. Argent. 76, 84–108.

Barzola, M., Tibaldi, A., Cristofolini, E., Otamendi, J., Demichelis, A., Armas, P., Camilletti, G., 2019b. Estructura interna de una sección de corteza media expuesta en el basamento metamórfico del sector centro-norte de Sierra de Comechingones, Córdoba, Argentina. Rev. Asoc. Geol. Argent. 76, 375–390.

Bence, A.E., Albee, A.L., 1968. Empirical correction factors for the electron microanalysis of silicates and oxides. J. Geol. 76, 382–403.

Berman, R.G., 1988. Mixing properties of Ca–Mg–Fe–Mn garnets. Am. Mineral. 75, 328–344.

Berman, R.G., Aranovich, L.Y., 1996. Optimized standard state and solution properties of minerals I. Model calibration for olivine, orthopyroxene, cordierite, garnet, and ilmenite in the system FeO–MgO–CaO–Al2O3–TiO2–SiO2. Contrib. Mineral. Petrol. 126, 1–24.

Black, L.P., Kamo, S.L., Allen, C.M., Davis, D.W., Aleinikoff, J.N., Valley, J.W., Mundil, R., Campbell, I.H., Korsch, R.J., Williams, I.S., Foudoulis, C., 2004. Improved Pb-206/U-218 microprobe geochronology by the monitoring of a trace-element-related matrix effect; SHRIMP, ID-TIMS, ELA-ICP-MS and oxygen isotope documentation for a series of zircon standards. Chem. Geol. 205, 115–140.

Brown, M., 1994. The generation, segregation, ascent and emplacement of granite magma: the migmatite-to-crustally-derived granite connection in thickened orogens. Earth Sci. Rev. 36, 83–130.

Brown, M., 2007. Crustal melting and melt extraction, ascent and emplacement in orogens: mechanism and consequences. J. Geol. Soc. 164, 709–730.
Brown, M., Solar, G.S., 1998. Shear-zone systems and melts: feedback relations and self-organization in orogenic belts. J. Struct. Geol. 20, 211–228.
Bucher, K., Grapes, R., 2011. Petrogenesis of Metamorphic Rocks. Springer-Verlag, Berlin Heidelberg, p. 441.
Casquet, C., Dahlquist, J., Verdecchia, S., Baldo, E., Galindo, C., Rapela, C., Pankhurst, R., Morales, M., Murra, J., Fanning, M., 2018. Review of the Cambrian Pampean orogeny of Argentina; a displaced orogen formerly attached to the Saldania Belt of South Africa? Earth Sci. Rev. 177, 209–225.
Clemens, J.D., Vielzeuf, D., 1987. Constraints on melting and magma production in the crust. Earth Planet Sci. Lett. 86, 287–306.
Collo, G., Astini, R., Cawood, P.A., Buchan, C., Pimentel, M., 2009. U–Pb detrital zircon ages and Sm–Nd isotopic features in low-grade metasedimentary rocks of the Famatina belt: implications for late Neoproterozoic–early Palaeozoic evolution of the proto-Andean margin of Gondwana. J. Geol. Soc. London 166, 303–319.
Coutts, D., Matthews, W., Hubbard, S., 2019. Assessment of widely used methods to derive depositional ages from detrital zircon populations. Geosci. Frontiers 10, 1421–1435.
Cristofolini, E.A., Otamendi, J.E., Ducea, M.N., Peason, D., Tibaldi, A.M., Baliani, I., 2012. Detrital zircon U-Pb ages of metasedimentary rocks from the sierra de Valle Fértil: revealing entrapment of late Cambrian marine successions into the deep roots of the early Ordovician Famatinian Arc. J. S. Am. Earth Sci. 37, 77–94.
Deer, W.A., Howie, R.A., Zussman, J., 1993. An Introduction to: the Rock Forming Minerals. Longman, England, p. 696.
Demartis, M., Jung, S., Berndt, J., Aragón, E., Sato, A.M., Radice, S., Maffini, M.N., Coniglio, J.E., Pinotti, L.P., D'Eramo, F.J., Insúa, L.A.A., 2017. Famatinian inner arc: petrographical observations and geochronological constraints on pegmatites and leucogranites of the Comechingones pegmatitic field (Sierras de Córdoba, Argentina). J. S. Am. Earth Sci. 79, 239–253.
Demichelis, A., Coniglio, J., Otamendi, J., Rabbia, O., 1996. Geology and petrology of Sol de Mayo-inti yaco metagabbro (Comechingones ranges, Córdoba). 13° Congreso Geológico Argentino, Actas 5, 413 (Buenos Aires).
D'Eramo, F., Esteban, J., Demartis, M., Aragón, E., Coniglio, J., Pinotti, L., 2020. Time lag between metamorphism and crystallization of anatectic granites (Córdoba, Argentina). Geol. Acta 18, 1–14.
Dickinson, W., Gehrels, G., 2009. Use of U-Pb ages of detrital zircons to infer maximum depositional ages of strata: a test against a Colorado Plateau Mesozoic database. Earth Planet Sci. Lett. 288, 115–125.
Drobe, M., López de Luchi, M.G., Steenken, A., Frei, R., Naumann, R., Wemmer, K., Siegesmund, S., 2011. The geodynamic evolution of the eastern Sierras Pampeanas. Int. J. Earth Sci. 100, 631–657.
Escayola, M., Pimentel, M.M., Armstrong, R., 2007. Neoproterozoic back-arc basin: sensitive high-resolution ion microprobe U-Pb and Sm-Nd isotopic evidence from the Eastern Pampean Ranges, Argentina. Geology 35, 495–498.
Gehrels, G., 2014. Detrital zircon U-Pb geochronology applied to tectonics. Annu. Rev. Earth Planet Sci. 42, 127–149.
Gehrels, G.E., Valencia, V.A., Ruiz, J., 2008. Enhanced precision, accuracy, efficiency, and spatial resolution of U-Pb ages by laser ablation – multicollector - inductively coupled plasma - mass spectrometry. G-cubed 9, Q03017. https://doi.org/10.1029/2007GC001805.
Gordillo, C., 1979. Observaciones sobre la petrología de las rocas cordieríticas de la Sierra de Córdoba. Bol. Acad. Nac. Cien. 53, 3–44.
Gordillo, C., 1984. Migmatitas cordieríticas de la Sierra de Córdoba, condiciones físicas de la migmatización. Acad. Nac. Cienc. (Cordoba Argent) Misc. 68, 1–40.
Gordillo, C., Lencinas, A., 1979. Sierras Pampeanas de Córdoba y san luis. In: Leanza, A. P. (Ed.), Geología Regional Argentina. Academia Nacional de Ciencias, Córdoba, pp. 577–650.
Gromet, L.P., Simpson, C., 1999. Age of the Paso del Carmen Pluton and implications for the durant of the Pampean Orogeny, Sierras de Córdoba, Argentina. 14° Congreso Geológico Argentino. Actas 1, 149–151 (Salta).
Guereschi, A., Martino, R., 2002. Geotermobarometría de la paragénesis cuarzo-plagioclasa-biotita-granate-sillimanita en gneises del sector centro-oriental de la sierra de Comechingones, Córdoba. Rev. Asoc. Geol. Argent. 57, 365–375.
Guereschi, A., Martino, R., 2008. Field and textural evidence of two migmatization events in the Sierras de Córdoba, Argentina. Gondwana Res. 13, 176–188.
Guereschi, A., Martino, R., 2014. Las migmatitas de las Sierras de Córdoba. In: Martino, R., Guereschi, A. (Eds.), Geología y Recursos Naturales de la Provincia de Córdoba. Relatorio del 19° Congreso Geológico Argentino, Córdoba, pp. 67–94.
Holland, T., Powell, R., 1992. Plagioclase feldspars: activity-composition relations based upon Darken's quadratic formalism and Landau theory. Am. Mineral. 77, 53–61.
Holland, T., Powell, R., 2011. An improved and extended internally consistent thermodynamic dataset for phases of petrological interest, involving a new equation of state for solids. J. Metamorph. Geol. 29, 333–383.
Hoskin, P.W.O., Schaltegger, U., 2003. The composition of zircon and igneous and metamorphic petrogenesis. In: Hanchar, J.M., Hoskin, P.W.O. (Eds.), Zircon: Mineralogical Society of America, vol. 53. Reviews in Mineralogy and Geochemistry, pp. 27–62.
Iannizzotto, N.F., Rapela, C.W., Baldo, E.G., Galindo, C., Fanning, C.M., Pankhurst, R.J., 2013. The sierra norte-Ambargasta batholiths: late Ediacaran-early Cambrian magmatism associated with Pampean transpressional tectonics. J. S. Am. Earth Sci. 42, 127–143.
Jackson, S.E., Pearson, N.J., Griffin, W.L., Belousova, E.A., 2004. The application of laser ablation-inductively coupled plasma-mass spectrometry to in situ U–Pb zircon geochronology. Chem. Geol. 211, 47–69.
Jordan, T., Allmendinger, R., 1986. The Sierras Pampeanas of Argentina: a modern analogue of Rocky Mountains foreland deformation. Am. J. Sci. 286, 737–764.
Kohn, M., Spear, F., 2000. Retrograde net transfer reaction insurance for pressure-temperature estimates. Geology 28, 1127–1130.
Kraemer, P.E., Escayola, M.P., Martino, R.D., 1995. Hipótesis sobre la evolución tectónica neoproterozoica de las Sierras Pampeanas de Córdoba (30°40'-32°40'), Argentina. Rev. Asoc. Geol. Argent. 50, 47–59.
Larrovere, M., Casquet, C., Aciar, H., Baldo, E., Alasino, P., Rapela, C., 2021. Extending the Pampean orogen in western Argentina: new evidence of Cambrian magmatism and metamorphism within the Ordovician Famatinian belt revealed by new SHRIMP U-Pb ages. J. S. Am. Earth Sci. 109, 103222. https://doi.org/10.1016/j.jsames.2021.103222.
Lee, A., Torvela, T., Lloyd, G., Walker, M., 2018. Melt organisation and strain partitioning in the lower crust. J. Struct. Geol. 113, 188–199.
Lira, R., Millone, H.A., Kirschbaum, A.M., Moreno, R.S., 1997. Calc-alkaline arc granitoid activity in the Sierra Norte-Ambargasta ranges, central Argentina. J. S. Am. Earth Sci. 10, 157–177.
Lira, R., Poklepovic, M.F., O'Leary, M.S., 2014. El magmatismo cámbrico en el batolito de Sierra Norte-Ambargasta. In: Martino, R., Guereschi, A. (Eds.), Geología y Recursos Naturales de la Provincia de Córdoba. Relatorio del 19° Congreso Geológico Argentino, Córdoba, pp. 183–215.
Ludwig, K.R., 2003. Isoplot 3.00, vol. 4. Berkeley Geochronology Center, Special Publication, 0-70.
Lyons, P., Skirrow, R.G., Stuart-Smith, P.G., 1997. Geology and metalogeny of the "Sierras Septentrionales de Córdoba". Geoscientific Mapping of the Sierras Pampeanas. In: t. Australian Geological Survey Organization, Subsecretaría de Minería de la Nación, p. 132, 1:250.000 map shee.
Martino, R., 2003. Las fajas de deformación dúctil de las Sierras Pampeanas de Córdoba: una reseña general. Rev. Asoc. Geol. Argent. 4, 549–571.
Martino, R., Guereschi, A., 2014. La estructura neoproterozoica-paleozoica inferior del complejo metamórfico de las Sierras Pampeanas de Córdoba. In: Martino, R., Guereschi, A. (Eds.), Geología y Recursos Naturales de la Provincia de Córdoba. Relatorio del 19° Congreso Geológico Argentino, Córdoba, pp. 95–128.
Martino, R., Escayola, M., Saal, A., 1994. Estructura del cuerpo de "kinzigita" del río Santa Rosa, Departamento Calamuchita, Provincia de Córdoba. Rev. Asoc. Geol. Argent. 49, 3–10.
Martino, R., Kraemer, P., Escayola, M., Giambastiani, M., Arnosio, M., 1995. Transecta de las Sierras Pampeanas de Córdoba a los 32°S. Rev. Asoc. Geol. Argent. 50, 60–77.
Martino, R., Guereschi, A., Giambastiani, M., 1997. El sinformal de la Sierra blanca: petrologia y evolucion estructural, sierra de Comechingones; Cordoba; Argentina. Rev. Asoc. Geol. Argent. 52, 41–46.
Martino, R.D., Guereschi, A.B., Anzil, P.A., 2010. Metamorphic and tectonic evolution at 31°36' S across a deep crustal zone from the sierra Chica of Cordoba, Sierras Pampeanas, Argentina. J. S. Am. Earth Sci. 30, 12–28.
Montel, J.M., Vielzeuf, D., 1997. Partial melting of metagreywackes. Part II: compositions of minerals and melts. Contrib. Mineral. Petrol. 128, 176–196.
Murra, J., Casquet, C., Locati, F., Galindo, C., Baldo, E., Pankhurst, R., Rapela, C., 2016. Isotope (Sr, C) and U-Pb SHRIMP zircon geochronology of marble-bearing sedimentary series in the Eastern Sierras Pampeanas, Argentina. Constraining the SW Gondwana margin in Ediacaran to early Cambrian times. Precambrian Res. 281, 602–617.
Northrup, C.J., Simpson, C., Gromet, I., 1998. Early Paleozoic history of the eastern Sierras Pampeanas, Argentina. 10° Congreso Latinoamericano de Geología, Actas 2, 400–403 (Buenos Aires).
Otamendi, J., Patiño Douce, A., 2001. Partial melting of aluminous metagreywackes in the northern sierra de Comechingones, central Argentina. J. Petrol. 42, 1751–1772.
Otamendi, J., Patiño Douce, A., Demichelis, A., 1999. Amphibolite to granulite transition in aluminous greywackes from the Sierra de Comechingones, Córdoba, Argentina. J. Metamorph. Geol. 17, 415–434.
Otamendi, J.E., Castellarini, P.A., Fagiano, M.R., Demichelis, A.H., Tibaldi, A.M., 2004. Cambrian to Devonian geologic evolution of the sierra de Comechingones, eastern Sierras Pampeanas, Argentina: evidence for the development and exhumation of continental crust on the proto-Pacific margin of Gondwana. Gondwana Res. 7, 1143–1155.
Otamendi, J., Cristofolini, E., Fagiano, M, Pinotti, L., D'Eramo, F., 2014. Los granitos devónicos del sur de la Sierra de Comechingones. In: Martino, R., Guereschi, A. (Eds.), Geología y Recursos Naturales de la Provincia de Córdoba. Relatorio del 19o Congreso. Geológico Argentino, Córdoba, pp. 277–291.
Otamendi, J., Barzola, M., Tibaldi, A., Cristofolini, E., Álvarez-Valero, A., Demichelis, A., 2019. Petrological and geochemical variations of a turbidite-like metasedimentary sequence over the metatexita to diatexite transition within the Pampean Orogen, Argentina. Int. J. Earth Sci. 108, 1361–1385.
Pankhurst, R., Rapela, C.W., Fanning, H., 2000. Age and origin of coeval TTG, I-and S-Type granites in the Famatinian belt of NW Argentina. Trans. R. Soc. Edinb. Earth Sci. 91, 151–168.
Patiño Douce, A.E., Beard, J.S., 1995. Dehydration-melting of biotite gneiss and quartz amphibolites from 3 to 15 kbar. J. Petrol. 36, 707–738.
Patiño Douce, A.E., Beard, J.S., 1996. Effects of P, $f(O_2)$ and Mg/Fe ratio on dehydration-melting of model metagreywackes. J. Petrol. 37, 999–1024.
Patiño Douce, A.E., Harris, N., 1998. Experimental constraints on Himalayan anatexis. J. Petrol. 39, 698–710.
Patiño Douce, A.E., Johnston, A.D., Rice, J., 1993. Octahedral excess mixing properties in biotite: a working model with applications to geobarometry and geothermometry. Am. Mineral. 78, 113–131.
Pattison, D.R.M., 1992. Stability of andalusite and sillimanite and the Al_2SiO_5 triple point: constraints from the Ballachulish aureole, Scotland. J. Geol. 100, 423–446.

Paton, C., Hellstrom, J., Paul, B., Woodhead, J., Hergt, J., 2011. Iolite: freeware for the visualisation and processing of mass spectrometric data. J. Anal. Atomic Spectrom. 26, 2508–2518.
Perón Orrillo, J.M., Suárez, A.O., Rivarola, D., Otamendi, J.E., Morosini, A., Romero, R., Leisen, M., Barra, F., 2019. Depositional age and provenance in the san luis formation, Sierras Pampeanas, Argentina: evidence from detrital zircon studies. J. S. Am. Earth Sci. 94, 102–228.
Rabbia, O., Demichelis, A., Otamendi, J., Coniglio, J., 1996. Evidences of pre-metamorphic within plate magmatism at Sierras de Córdoba, eastern Pampean ranges, Argentina. 13° Congreso Geológico Argentino, simposio: proto-Andean margin of Gondwana. Actas 5, 441 (Buenos Aires).
Radice, S., Sola, A., Maffini, N., D'Eramo, F., Weinberg, R., Pinotti, L., Demartis, M., Coniglio, J., Boffadossi, A., Muratori, M.E., 2021. Constraining the timing and evolution of a long-lived tectonic boundary: an example from the Early Paleozoic, Argentina. J. S. Am. Earth Sci. https://doi.org/10.1016/j.jsames.2020.102892.
Ramos, A.M., 1979. Rocas básicas y gneises asociados en la comarca de Río Grande, Departamento Calamuchita, Provincia de Córdoba. Boletín Academia Nacional de Ciencias 53, 143–165.
Ramos, V.A., 1988. Late Proterozoic-early Paleozoic of South America - a collisional history. Episodes 11–3, 168–174.
Ramos, V.A., Escayola, M., Leal, P., Pimentel, M.M., Santos, J., 2015. The late stages of the Pampean Orogeny, Córdoba (Argentina): evidence of postcollisional Early Cambrian slab break-off magmatism. J. S. Am. Earth Sci. 64, 351–364.
Rapela, C., Pankhurst, R., Casquet, C., Baldo, E., Saavedra, J., Galindo, C., Fanning, C., 1998. The Pampean Orogeny of the southern proto-Andes: Cambrian continental collision in the Sierras de Córdoba. In: Pankhurst, R., Rapela, C. (Eds.), The Proto-Andean Margin of Gondwana, vol. 142. Geological Society, Special Publications, London, pp. 181–217.
Rapela, C.W., Pankhurst, R.J., Casquet, C., Fanning, C.M., Baldo, E.G., González-Casado, J.M., Galindo, C., Dahlquist, J., 2007. The Río de la Plata craton and the assembly of SW Gondwana. Earth Sci. Rev. 83, 49–82.
Rapela, C.W., Verdecchia, S.O., Casquet, C., Pankhurst, R.J., Baldo, E.G., Galindo, C., Murra, J.A., Dahlquist, J.A., Fanning, C.M., 2016. Identifying laurentian and SWGondwana sources in the neoproterozoic to early Paleozoic metasedimentary rocks of the Sierras Pampeanas: Paleogeographic and tectonic implications. Gondwana Res. 32, 193–212.
Sawyer, E.W., 1994. Melt segregation in the continental crust. Geology 22, 1019–1022.
Sawyer, E.W., 2001. Melt segregation in the continental crust: distribution and movement of melt in anatectic rocks. J. Metamorph. Geol. 19, 291–309.
Sawyer, E.W., 2008. Atlas of Migmatites. NRC Research Press, Québec, p. 371.
Schwartz, J.J., Gromet, L.P., 2004. Provenance of a Proterozoic-early Cambrian basin, Sierras de Córdoba, Argentina. Precambrian Res. 129, 1–21.
Schwartz, J., Gromet, L., Miró, R., 2008. Timing and duration of the calcalkaline arc of the Pampean orogeny: implication for the late-neoproterozoic to Cambrian evolution of western Gondwana. J. Geol. 116, 39–61.
Semenov, I., Weinberg, R.F., 2017. A major mid-crustal decollement of the Paleozoic convergent margin of Western Gondwana: the Guacha Corral shear zone, Argentina. J. Struct. Geol. 103, 75–99.
Semenov, I., Weinberg, R., Taylor, R., Jourdan, F., 2019. Prolonged movement on a > 10-km-wide thrust during early Paleozoic orogens in the Gondwana margin of NW Argentina. Tectonics 38, 3210–3236.
Siegesmund, S., Steenken, A., Martino, R.D., Wemmer, K., López de Luchi, M.G., Frei, R., Presnyakov, S., Guereschi, A., 2010. Time constraints on the tectonic evolution of the eastern Sierras Pampeanas (central Argentina). Int. J. Earth Sci. 99, 1199–1226.
Simpson, C., Law, R.D., Gromet, L.P., Miro, R., Northrup, C.J., 2003. Paleozoic deformation in the Sierras de Córdoba and sierra de La Minas, eastern Sierras Pampeanas, Argentina. J. S. Am. Earth Sci. 15, 749–764.
Sims, J., Ireland, T., Camacho, A., Lyons, P., Pieters, P., Skirrow, R., Stuart-Smith, P., Miró, R., 1998. U-Pb and Ar-Ar geochronology from the southern Sierras Pampeanas, Argentina: implications for the Paleozoic tectonic evolution of the western Gondwana margin. In: Pankhurst, R., Rapela, C. (Eds.), The Proto-Andean Margin of Gondwana, vol. 142. Geological Society, Special Publications, London, pp. 259–281.
Slama, J., Košler, J., Condon, D., Crowley, J., Gerdes, A., Hanchar, J., Horstwood, M., Morris, G., Nasdala, L., Norberg, N., Schaltegger, U., Schoene, B., Tubrett, M., Whitehouse, M., 2008. Plešovice zircon - a new natural reference material for U–Pb and Hf isotopic microanalysis. Chem. Geol. 249, 1–35.
Spear, F.S., 1993. Metamorphic Phase Equilibria and Pressure-Temperature-Time Paths. Mineralogical Society of America, Washington, D. C, p. 799.
Spear, F., Kohn, M., Cheney, J., 1999. P-T paths from anatectic pelites. Contrib. Mineral. Petrol. 134, 17–32.
Steenken, A., Wemmer, K., Martino, R.D., Lopez de Luchi, M.G., Guereschi, A., Siegesmund, S., 2010. Post-pampean cooling and the exhumation of the Sierras Pampeanas in the west of Cordoba. (Central Argentina). Neues Jahrbuch fur Geologie und Palaontologie 256, 235–255.
Stuart-Smith, P.G., Miro, R., Camacho, A., Sims, J.P., Skirrow, R.G., Lyons, P., Pieters, P. E., Black, L.P., 1999. Uranium–lead dating of felsic igneous cycles in the southern Sierras Pampeanas, Argentina: implications for the tectonic development of the proto-Andean Gondwana margin. In: Ramos, V.A., Keppie, D. (Eds.), Laurentia Gondwana Connections before Pangea, vol. 336. Geological Society of America, Special Paper, pp. 87–114.
Thompson, A.B., 1996. Fertility of crustal rocks during anatexis. Trans. R. Soc. Edinb. Earth Sci. 87, 1–10.
Tibaldi, A.M., Otamendi, J.E., Gromet, L.P., Demichelis, A.H., 2008. Suya Taco and Sol de Mayo mafic complexes from eastern Sierras Pampeanas, Argentina: evidence for the emplacement of primitive OIB-like magmas into deep crustal levels at a late stage of the Pampean orogeny. J. S. Am. Earth Sci. 26, 172–187.
Tibaldi, A., Demichelis, A., Fagiano, M., Otamendi, J., Rabbia, O., 2014. Las rocas máficas del paleozoico inferior de las Sierras de Córdoba. In: Martino, R., Guereschi, A. (Eds.), Geología y Recursos Naturales de la Provincia de Córdoba. Relatorio del 19° Congreso Geológico Argentino, Córdoba, pp. 151–167.
Tibaldi, A., Barzola, M., Cristofolini, E., Otamendi, J., Demichelis, A., Leisen, M., Romero, R., Barra, F., Camilletti, G., Armas, P., 2019. Syn-deformational anatexis along the Santa Rosa river section, Argentina: feedback relation between deformation, metamorphism and melt extraction. J. Struct. Geol. 124, 151–167.
Tibaldi, A., Otamendi, J., Demichelis, A., Barzola, M., Barra, F., Rabbia, O., Cristofolini, E., Benito, M.P., 2021. Early Cambrian multiple-sourced plutonism in the eastern Sierras Pampeanas, Córdoba, Argentina: implications for the evolution of the early Paleozoic Gondwana margin. J. S. Am. Earth Sci. 106, 103048. https://doi.org/10.1016/j.jsames.2020.103048.106.
Verdecchia, S., Casquet, C., Baldo, E.G., Pankhurst, R.J., Rapela, C.W., Fanning, M., Galindo, C., 2011. Mid- to Late Cambrian docking of the Río de la Plata craton to southwestern Gondwana: age constraints from U–Pb SHRIMP detrital zircon ages from Sierras de Ambato and Velasco (Sierras Pampeanas, Argentina). J. Geol. Soc. London 168, 1061–1071.
Vernon, R., White, R., Clarke, G., 2008. False metamorphic events inferred from misinterpretation of microstructural evidence and P-T data. J. Metamorph. Geol. 26, 437–449.
Vielzeuf, D., Montel, J., 1994. Partial melting of metagreywackes, I, Fluid-absent experiments and phase relationships. Contrib. Mineral. Petrol. 118, 375–394.
Von Gosen, W., Prozzi, C., 2010. Pampean deformation in the Sierra Norte de Córdoba, Argentina: implications for the collisional history at the western pre-Andean Gondwana margin. Tectonics 29, 1–33.
Von Gosen, W., McClelland, W., Loske, W., Martinez, J., Prozzi, C., 2014. Geochronology of igneous rocks in the sierra norte de Córdoba (Argentina): implications for the Pampean evolution at the western Gondwana margin. Lithosphere 6, 277–300.
Whitmeyer, S.J., Simpson, C., 2003. High strain-rate deformation fabrics characterize a kilometers-thick Paleozoic fault zone in the Eastern Sierras Pampeanas, central Argentina. J. Struct. Geol. 25, 909–922.
Whitney, D., Evans, B., 2010. Abbreviations for names of rock-forming minerals. Am. Mineral. 95, 185–187.
Wiedenbeck, M., Alle, P., Corfu, F., Griffin, W.L., Meier, M., Oberli, F., Von Quadt, A., Roddick, J.C., Spiegel, W., 1995. Three natural zircon standards for U-Th-Pb, Lu-Hf, trace element and REE analyses. Geostand. Newsl. 19, 1–23.
Wiedenbeck, M., Hanchar, J., Peck, W., Sylvester, P., Valley, J., Whitehouse, M., Kronz, A., Morishita, Y., Nasdala, L., Fiebig, J., Franchi, I., Girard, J.-P., Greenwood, R., Hinton, R., Kita, N., Mason, P., Norman, M., Ogasawara, M., Piccoli, P., Rhede, D., Satoh, H., Schulz-Dobrick, B., Skar, O., Spicuzza, M., Terada, K., Tindle, A., Togashi, S., Vennemann, T., Xie, Q., Zheng, Y., 2004. Further char-acterisation of the 91500 zircon crystal. Geostand. Geoanal. Res. 28, 9–39.
Williams, I.S., 1998. U–Th–Pb geochronology by ion microprobe. In: McKibben, M.A., Shanks, W.C.I.I.I., Ridley, W.I. (Eds.), Applications of Microanalytical Techniques to Understanding Mineralizing Processes, vol. 7. Reviews of Economic Geology, pp. 1–35.
Yakymchuk, C., Kirkland, C., Clark, C., 2018. Th/U ratios in metamorphic zircon. J. Metamorph. Geol. 36, 715–737.
Yardley, B.W.D., 1977. An empirical study of diffusion in garnet. Am. Mineral. 62, 793–800.